



## Review

## Photocatalytic Cr(VI) reduction in metal-organic frameworks: A mini-review

Chong-Chen Wang<sup>a,b,\*</sup>, Xue-Dong Du<sup>a</sup>, Jin Li<sup>a</sup>, Xin-Xing Guo<sup>a</sup>, Peng Wang<sup>a</sup>, Jia Zhang<sup>a</sup><sup>a</sup> Key Laboratory of Urban Stormwater System and Water Environment (Ministry of Education), Beijing University of Civil Engineering and Architecture, Beijing, 100044, China<sup>b</sup> Beijing Engineering Research Centre of Sustainable Urban Sewage System Construction and Risk Control, Beijing University of Civil Engineering and Architecture, Beijing, 100044, China

## ARTICLE INFO

## Article history:

Received 28 February 2016

Received in revised form 13 April 2016

Accepted 14 April 2016

Available online 19 April 2016

## Keywords:

Metal-organic frameworks

Photocatalysis

Visible light

Cr(VI) reduction

Review

## ABSTRACT

This mini-review presented photocatalytic reduction of Cr(VI) into Cr(III) in some MOFs or their derivatives/composites. The reported examples are collected and analyzed; and the reaction mechanism, the influence of various factors on the photocatalytic performance, the involved challenges, and the outlooks of MOFs as photocatalyst to carry out Cr(VI) reduction are discussed. It can be found that the optical properties of MOFs can be flexible modulated via incorporation into  $-NH_2$  group, conductor photocatalysts like ZnO and metal sulfides nanoparticles, noble metal nanoparticles and graphene oxide (GO). It is clear that MOFs have a bright prospective in the fields of photocatalytic reduction of Cr(VI), or even dual functional photocatalysts to carry out Cr(VI) reduction and organic pollutants degradation under visible light irradiation.

© 2016 Elsevier B.V. All rights reserved.

## Contents

1. Introduction .....	198
2. The current status of photocatalytic Cr(VI) reduction in MOFs .....	199
2.1. MOFs photocatalyst .....	199
2.1.1. $NH_2$ -MIL-125(Ti) .....	199
2.1.2. UiO-66( $NH_2$ ) .....	202
2.1.3. $NH_2$ -MIL-88B(Fe), $NH_2$ -MIL-53(Fe) and $NH_2$ -MIL-101(Fe) .....	203
2.2. Semiconductor/MOFs hybrid photocatalysts .....	204
2.2.1. $Me_xS_y @ MIL-125(Ti)$ ( $Me_xS_y = CdS, In_2S_3, SnS_2, Sb_2S_3$ ) .....	204
2.2.2. $ZnO@ZIF-8$ .....	205
2.3. Conductor/MOFs hybrid photocatalysts .....	208
2.3.1. $Pd@UiO-66(NH_2)$ .....	208
2.3.2. $RG@UiO-66(NH_2)$ .....	210
3. Challenges and outlooks .....	214
Acknowledgements .....	214
Appendix A. Supplementary data .....	214
References .....	214

\* Corresponding author at: Key Laboratory of Urban Stormwater System and Water Environment (Ministry of Education), Beijing University of Civil Engineering and Architecture, Beijing, 100044, China.

E-mail address: [chongchenwang@126.com](mailto:chongchenwang@126.com) (C.-C. Wang).

## 1. Introduction

Heavy metals have been used by humans for thousands of years, and more exposure to heavy metals continues, even increases in some countries, which results in several adverse health effects [1]. Among the toxic heavy metal ions, hexavalent chromium (Cr(VI)) is a common contaminant in surface and ground water, as it is widely

utilized in leather tanning, electroplating, printing, pigments, polishing and other industries [2–4]. The existence of Cr(VI) in aquatic system and drinking water sources can increase the threat of severe diarrhea and liver, kidney and skin cancers, due to its acute toxicity to most of organism strong carcinogenic property and its high solubility in water [5–9]. Different from other common heavy metals like lead, cadmium, and copper, chromium primarily presents in both low-toxic form of Cr(III) and high toxic Cr(VI). The United States Environmental Protection Agency (US EPA) set maximum contaminant limits for total chromium in drinking water of  $100 \mu\text{g L}^{-1}$  and the World Health Organization (WHO) set a stricter threshold of  $50 \mu\text{g L}^{-1}$ . As a result, the removal of Cr(VI) from water is required at any cost. Various methods including but not limited to chemical precipitation [10,11], adsorption [12–16], membrane filtration [17] and reduction from highly toxic Cr(VI) to lowly toxic Cr(III) [9,18–26] have been reported for the wastewater treatment. One of the most preferred methods to perform effective remediation of Cr(VI)-contaminated wastewater is the transformation of Cr(VI) to Cr(III), because Cr(III) is lowly toxic and can be easily precipitated and removed as a solid waste like  $\text{Cr}(\text{OH})_3$ . Compared with electro-reduction [27–30], chemical reduction [31–33], and micro-reduction [34–36], photocatalytic reduction of Cr(VI) to Cr(III) using photocatalysts is more effective and low-cost, as well as does not produce any hazardous chemicals [9,18–26]. Generally,  $\text{TiO}_2$  was used to conduct photocatalytic Cr(VI) reduction due to its durability, low cost, low toxicity, superhydrophilicity, and remarkable chemical and photochemical stability [20,25,26,37–39]. However, the application of  $\text{TiO}_2$  is limited by its disadvantages like low photocurrent quantum yield due to electron–hole recombination, low solar energy utilization efficiency (no more than 5% UV light in solar light) resulting from the narrow band gap ( $E_g = 3.0 - 3.2 \text{ eV}$ ), difficult post-separation after water treatment, along with agglomeration due to its fine particle size and large surface area-to-volume ratio [40,41]. In recent years, to achieve efficient utilization of the sunlight, great efforts have been devoted to searching for other photocatalysts which can exhibit high efficient Cr(VI) reduction under visible light irradiation. Up to now,  $\text{CdS}$ ,  $\text{SnS}_2$ ,  $\text{Ag}_2\text{S}$  and  $\text{WO}_3$  have been widely used to carry out photocatalytic reduction of Cr(VI) upon the visible light illumination [18,23,42–44], but also suffer from their poor reduction efficiency and slow reduction rate [45]. Furthermore, in order to convert solar energy to chemical energy, some artificial systems and devices using inorganic and organic materials have been developed recently [46–50], in which three fundamental steps are needed: (i) sunlight absorption by photosensitizers to mediate charge-separated excited states; (ii) generation of redox equivalents and their migration to reactive sites, and (iii) reduction and oxidation half reactions with the redox equivalents (electrons and holes) at the catalytic centres [51,52]. Consequently, it is of urgency to look for new visible-light active photocatalysts with stable and high photocatalytic ability for the Cr(VI) reduction.

Metal-organic frameworks (MOFs), as a newly emerged type of functional inorganic–organic hybrid materials, serve as an interesting platform to design and study artificial photosynthetic systems. Generally, MOFs can contain both photosensitizers and catalytic centres in a single solid, which provide the structural organization to integrate the three fundamental steps of artificial photosynthesis stated-above into a single material [51]. Recently, MOFs have attracted significant research attentions due to their diverse and easily tailored structures [53–58], as well as various potential applications, such as in catalysis [59–66], gas separation [67–73], gas storage [61,74–78], carbon dioxide capture and transformation [52,79–82], and so on [53–58,67–70,83–86]. Also, the application of MOFs in heterogeneous photocatalysis under UV/visible/UV–vis irradiation for water splitting and  $\text{CO}_2$  reduction by using photogenerated electrons, and degrading organic pollutants based on holes have emerged widely [63,87–97]. Their

high photocatalytic performance can contribute to the richness of metal-containing nodes as catalytically active sites, functional organic linkers, the easily tailorable physical and chemical functions, the large surface area and permanent pores/channels to potentially anchor/encapsulate photosensitizers and catalytic moieties, small metal-oxide cluster as well as tuneable band gap [90,98,99]. Compared with the traditional photocatalysts, the advantage of the MOFs as photocatalysts results from their desirable topology and high surface area, which can facilitate the fast transport and good accommodation of targeted molecules [45]. Especially, the MOFs' band gap is closely related to the HOMO–LUMO gap, and energy transfer can take place from the organic linker to the metal-oxo cluster within some MOFs under light irradiation [100], which can be further tuned to achieve efficient light harvest via rational modification of the inorganic unit or organic linkers [101]. Several review articles had highlighted the research progress of MOFs as photocatalysts to perform water splitting [61,88,102,103],  $\text{CO}_2$  reduction [52], and organic pollutants degradation [89,98,103–105], but up to now, no researcher focused to collect the research progress on photocatalytic Cr(VI) reduction in metal-organic frameworks. In fact, the study of MOF applications in this topic thus has a bright future although it is not so widely explored to date.

## 2. The current status of photocatalytic Cr(VI) reduction in MOFs

The research progress of MOFs applications in photocatalytic Cr(VI) reduction was highlighted as listed in Table 1. Some typical amine-functionalized MOFs (like MIL-125( $\text{NH}_2$ ), UiO-66( $\text{NH}_2$ ) and MIL-88B( $\text{Fe}$ )), semiconductor/MOFs composites (such as  $\text{CdS@MIL-125}(\text{NH}_2)$  and  $\text{ZnO@ZIF-8}$ ) and conductor/MOFs composites (like  $\text{Pd@UiO-66}(\text{NH}_2)$  and  $\text{RGO@UiO-66}(\text{NH}_2)$ ) were selected to be interpreted in detail; the involved reaction mechanism and the influence of various factors on the catalytic performance are discussed; as well as the involved challenges and the prospects are estimated.

### 2.1. MOFs photocatalyst

Generally, metal-organic frameworks (MOFs) exhibit semiconductor-like behavior upon the light irradiation, as their organic linkers can act as antennas to harvest light and subsequently active the metal sites via ligand to metal charge transition (LMCT) [98,117,118]. MOFs were often used as photocatalysts to conduct artificial photosynthetic reactions, due to that excited MOFs can generate electrons and holes which can subsequently be transferred to the surface to irrigate heterogeneous photoredox reactions [52,89,119–122]. Unfortunately, most MOFs can be used as efficient photocatalysts only under the UV light irradiation, which limited their wide application. It is commonly accepted that the introduction of amine ( $-\text{NH}_2$ ) group into MOFs can improve the photocatalytic performance. The amine ( $-\text{NH}_2$ )-functionalized MOFs show extra absorption band edge falling in the visible region, because the amine group can enhance both the electron transfer from the excited amine functionalized organic linker to oxo-metal clusters and the direct excitation of oxo-metal cluster [45,88,123–125].

#### 2.1.1. $\text{NH}_2$ -MIL-125(Ti)

Based on the linker-to-cluster charge-transfer mechanism, MOFs constructed from Ti centres are expected to be candidates to conduct the Cr(VI) reduction, as the titanium-oxo cluster can facilitate efficient charge transfer from the excited state of organic linker to the cluster. MIL-125(Ti) ( $\text{Ti}_8\text{O}_8(\text{OH})_4(\text{BDC})_6$ , BDC = benzene-1,4-dicarboxylate) was a good example, because of its large surface area, adjustability and photo-responsiveness [126]. Different from

**Table 1**

Performance of some typical metal-organic frameworks (or their composites) as photocatalysts for the reduction of Cr(VI) under visible light irradiation.

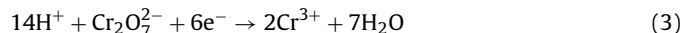
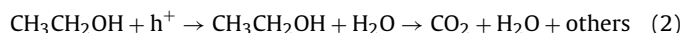
Photocatalyst/amount (mg)	Cr(VI) solution Volume (mL)/concentration (ppm)/pH	Time (min)	Reduction efficiency (%)	Ref.
NH <sub>2</sub> -MIL-125(Ti)/20	50/48/2.1	60	97	[106]
UiO-66(NH <sub>2</sub> )/20	40/10/2.0	80	97	[101,107]
NH <sub>2</sub> -MIL-88B (Fe)/20	40/8/2.0	50	100	[45]
MIL-101(Fe)/20	40/8/2.0	60	100	[45]
MIL-68(In)-NH <sub>2</sub> /40	40/20/2.0	180	97	[108]
MIL-53(Fe)/40	40/20/3.0	40	100	[109]
CuS@ MIL-125(Ti)/25	50/48/2.1	70	52	
ZnO@ZIF-8/20	20/20/7.0	80	100	[110]
RGO-UiO-66(NH <sub>2</sub> )/20	40/10/2.0	100	100	[111]
Pd@UiO-66(NH <sub>2</sub> )/20	40/10/2.0	90	100	[112]
MIL-53(Fe)-RGO/40	40/20/4.0	80	100	[113]
Pd-Cu/MIL-101/100	5/5580/0.3 mL HCOOH	60	100	[114]
2 wt% Pt@MIL-101/27.5	5/5580/0.3 mL HCOOH	40	100	[115]
2 wt% Pd@MIL-101/15	5/5580/0.3 mL HCOOH	210	100	[115]
HPMo@MIL-100(Fe)/20	40/20/4.0	8	100	[116]

MIL-125(Ti) which can only be photo-excited under UV light irradiation, NH<sub>2</sub>-MIL-125(Ti) built up from 2-aminoterephthalate (ATA, the derivative of BDC) can be irradiated under visible light, making it to efficiently utilize the solar energy. The introduction of –NH<sub>2</sub> group can significantly influence O to Ti charge transfer (LMCT) in TiO<sub>5</sub>(OH) inorganic cluster, resulting into that NH<sub>2</sub>-MIL-125(Ti) shows an extra absorption band edge at around 520 nm, significant red shift from absorption band edge at 350 nm of MIL-125(Ti) [52].

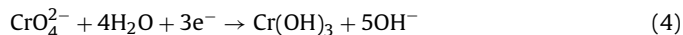
To investigate the performance of photocatalytic Cr(VI) reduction over visible-light active NH<sub>2</sub>-MIL-125(Ti), Wang and co-workers prepared NH<sub>2</sub>-MIL-125(Ti) with a modified solvo-thermal method, along with MIL-125(Ti) [106,125]. The morphologies of MIL-125(Ti) and NH<sub>2</sub>-MIL-125(Ti) were depicted in Fig. 1(a) and (b), in which the well crystallized white MIL-125(Ti) powder possesses the particle size distribution of ~2 μm, while the yellow NH<sub>2</sub>-MIL-125(Ti) powder exhibit analogous microcosmic morphology with the particle size 400–600 nm. The XRD patterns and the XPS measurement of NH<sub>2</sub>-MIL-125(Ti) and MIL-125(Ti) are nearly identical, indicating that the introduction of –NH<sub>2</sub> groups in the organic linkers does not alter the crystal lattice structure and the electronic structures of MIL-125(Ti), as illustrated in Fig. 1(c) and (d). No signals of characteristic peaks corresponding to bulk titanium dioxide phases, like anatase and rutile, are detected in the XRD pattern of NH<sub>2</sub>-MIL-125(Ti), implying that no bulky aggregated titanium oxide species were presented in the as-prepared NH<sub>2</sub>-MIL-125(Ti) [106]. The UV–vis DRS spectrum results revealed that MIL-125(Ti) and NH<sub>2</sub>-MIL-125(Ti) show absorption bands below 350 nm and 520 nm, respectively, in which the introduction of 2-aminoterephthalate ligand shifts the photo-absorption edge from UV light of MIL-125(Ti) to the visible light region of NH<sub>2</sub>-MIL-125(Ti), leading to more efficient solar energy utilization, as illustrated in Fig. 1(e) and (f).

NH<sub>2</sub>-MIL-125(Ti) can achieve better Cr(VI) reduction performance than MIL-125(Ti) under visible light, as listed in Fig. 2(a). To obtain optimum photocatalytic reaction conditions, the effects of different hole scavengers and pH values on the photocatalytic activities were studied. At pH=2.1, it was found that the addition of ethanol as hole scavenger can enhance the photocatalytic activities of NH<sub>2</sub>-MIL-125(Ti) on Cr(VI) reduction from 76% without any hole scavengers to 91%, while the addition of citric acid and EDTA as hole scavengers decreases the photocatalytic efficiency of Cr(VI) reduction to 72% and 66% under the same condition, respectively, as illustrated in Fig. 2(b). Ethanol was assumed to be absorbed onto the surface of NH<sub>2</sub>-MIL-125(Ti), which facilitate it to be mineralized facily in the reaction system [108,127]. As illustrated in Fig. 2(c), the Cr(VI) reduction efficiency increased with the ethanol concentration, because reducing radicals formed from ethanol can capture

the photo-induced holes over NH<sub>2</sub>-MIL-125(Ti) (as listed in Eqs. (1)–(3)). Therefore, more electrons can escape from the pair recombination to enhance Cr(VI) reduction under the acid condition. While the carboxylic groups attached on citric acid and EDTA were ready to form hydrogen bonding interactions with –NH<sub>2</sub> group of the photocatalyst to enhance the electrostatic adsorption effect between the Cr(VI) anion and the positively charged nitrogen on the photocatalytic reduction reaction, which limited the acceptance of the photogenerated electrons over Ti sites in NH<sub>2</sub>-MIL-125(Ti) resulting into decrease of the Cr(VI) reduction efficiency.



The Cr(VI) reduction efficiency over NH<sub>2</sub>-MIL-125(Ti) decreased rapidly from 91% to 63%, 47% and 24% with the pH values increased from 2.10 to 4.07, 6.04 and 8.17, respectively, as shown in Fig. 2(d). Under the acidic conditions, the photocatalytic reaction of Cr(VI) occurs following Eq. (3), and the existence of abundant H<sup>+</sup> facilitates the photocatalytic Cr(VI) reduction. While in alkaline medium, the corresponding chemical reaction proceeds following Eq. (4) as CrO<sub>4</sub><sup>2-</sup> is predominant. The zeta potentials of MIL-125(Ti) and NH<sub>2</sub>-MIL-125(Ti) become more negative with the increase of pH values. The zeta potential of NH<sub>2</sub>-MIL-125(Ti) became positive when the pH values is below 4.6 (the isoelectric point of NH<sub>2</sub>-MIL-125(Ti)). Hence, the positive surface can provide better adsorption performance for anionic Cr(VI), enhancing the capture of photo-generated electron to achieve higher Cr(VI) photoreduction efficiency under acid conditions. While the higher pH values made the surface of catalyst negative, leading to electrostatic repel the anionic Cr(VI) and readily adsorption of the cationic Cr(III) [127]. Furthermore, the formed Cr(III) will be precipitated into Cr(OH)<sub>3</sub> at pH > 6, which will mask the active sites of NH<sub>2</sub>-MIL-125(Ti) catalyst.



XPS was introduced to confirm the valence state of Cr bound to NH<sub>2</sub>-MIL-125(Ti). As illustrated in Fig. 3(a), the peaks of Cr 2p<sub>3/2</sub> orbitals (577.3 eV and 580.7 eV) can be assigned to Cr(III), implying that Cr(VI) was reduced into Cr(III). While the peak of Cr 2p<sub>3/2</sub> orbitals (586.7 eV) can be attributed to Cr(VI) absorbed onto NH<sub>2</sub>-MIL-125(Ti) due to its large surface area, pore structure and electrostatic interaction, which can be confirmed by the fact of N 1s peak shift from 402.6 eV of NH<sub>2</sub>-MIL-125(Ti) to 401.1 eV over Cr/NH<sub>2</sub>-MIL-125(Ti) [128]. Considering the observations of the XPS spectrum, a possible mechanism of the photocatalytic Cr(VI) reduction over NH<sub>2</sub>-MIL-125(Ti) was proposed, as illustrated in

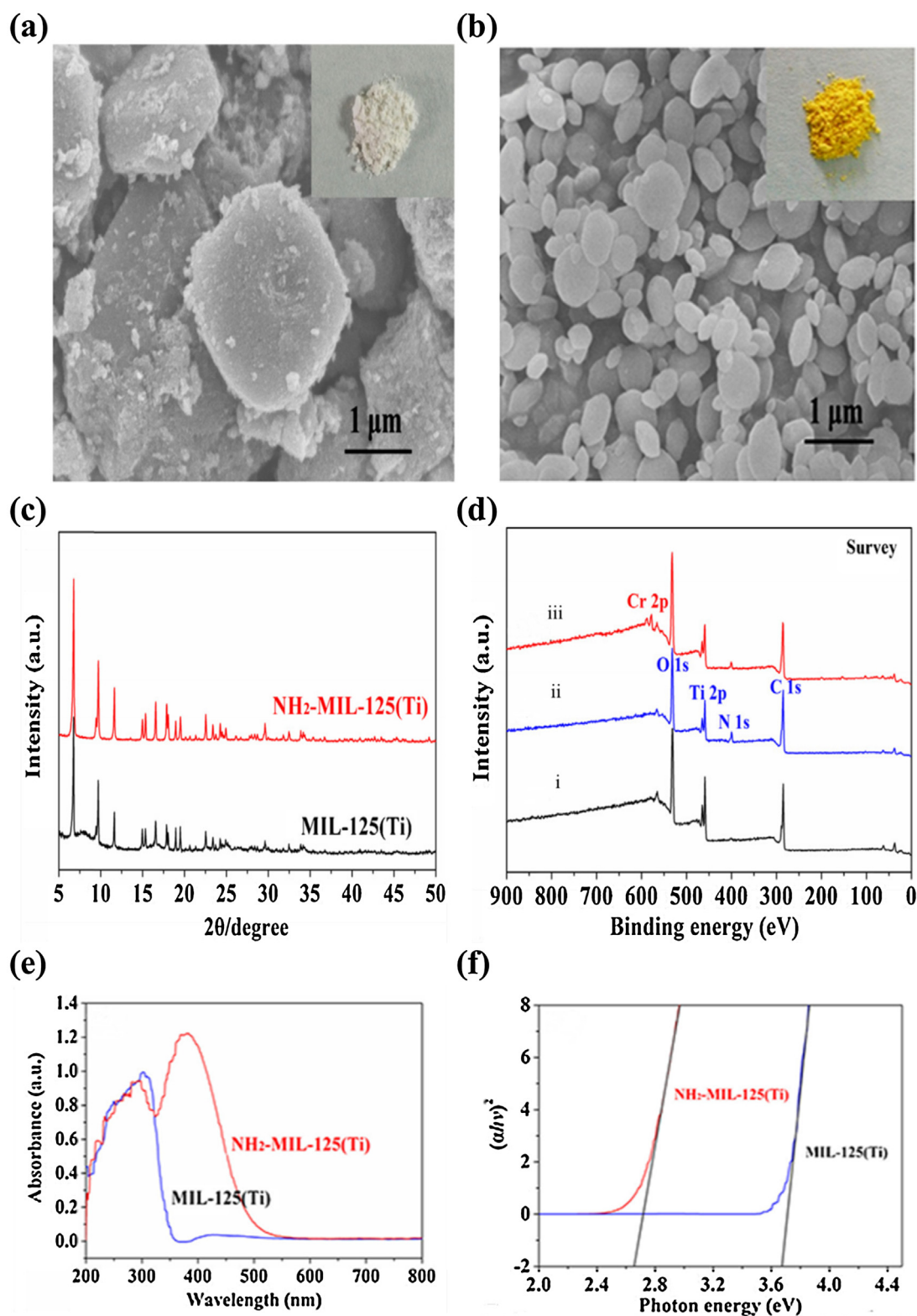


**Fig. 1.** (a) and (b) SEM images of MIL-125(Ti) and NH<sub>2</sub>-MIL-125(Ti). The inset is the corresponding photograph. (c) XRD patterns of MIL-125(Ti) and NH<sub>2</sub>-MIL-125(Ti); (d) the XPS spectra of (i) MIL-125(Ti), (ii) NH<sub>2</sub>-MIL-125(Ti) and (iii) NH<sub>2</sub>-MIL-125(Ti) photocatalyst after photocatalytic reaction. (e) UV-vis spectrum and (f) plot of  $(\alpha h\nu)^2$  versus photon energy ( $h\nu$ ) of the NH<sub>2</sub>-MIL-125(Ti) and the MIL-125(Ti) [106], copyright (2015) Elsevier.

Fig. 3(b). The H<sub>2</sub>ATA in NH<sub>2</sub>-MIL-125(Ti) played a role of antenna to enhance the absorption of visible light, and the excited H<sub>2</sub>ATA can transfer the photo-generated electrons to titanium-oxo cluster to produce Ti<sup>3+</sup> species, which can be quickly re-oxidized to

Ti<sup>4+</sup> after exposure to air [123,125]. The Ti<sup>3+</sup>-Ti<sup>4+</sup> intervalence charge transfer in titanium oxo-clusters was clarified by Horiuchi et al. with the aid of both electron spin resonance (ESR) spectrum and the UV-vis spectrum [125]. The ethanol adsorbed on



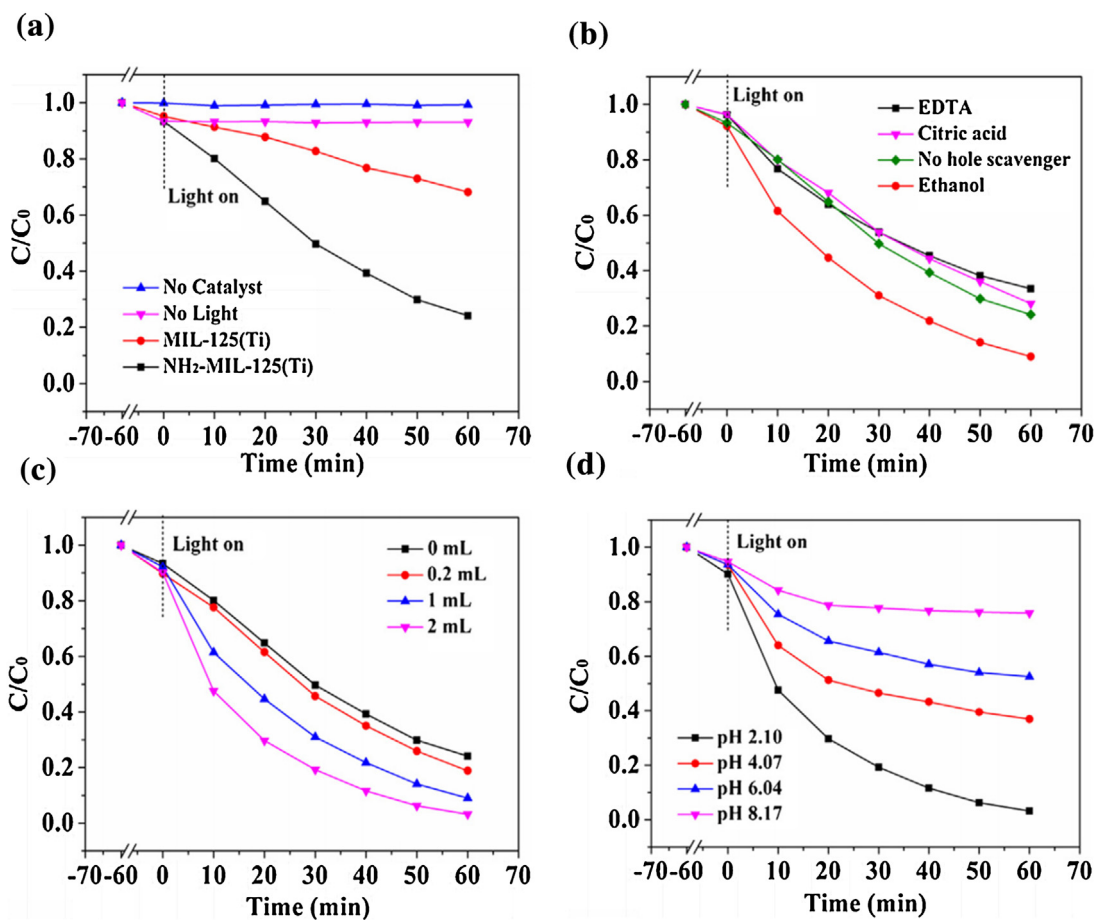


**Fig. 2.** (a) Reaction profiles of photocatalytic reduction of Cr(VI); (b) photocatalytic activities of NH<sub>2</sub>-MIL-125(Ti) for Cr(VI) reduction in the presence of various hole scavengers; (c) photocatalytic activities of NH<sub>2</sub>-MIL-125(Ti) for the reduction of Cr(VI) with different ethanol concentration; (d) photocatalytic activities of NH<sub>2</sub>-MIL-125(Ti) for the Cr(VI) reduction in aqueous solution at different pH values [106], copyright (2015) Elsevier.

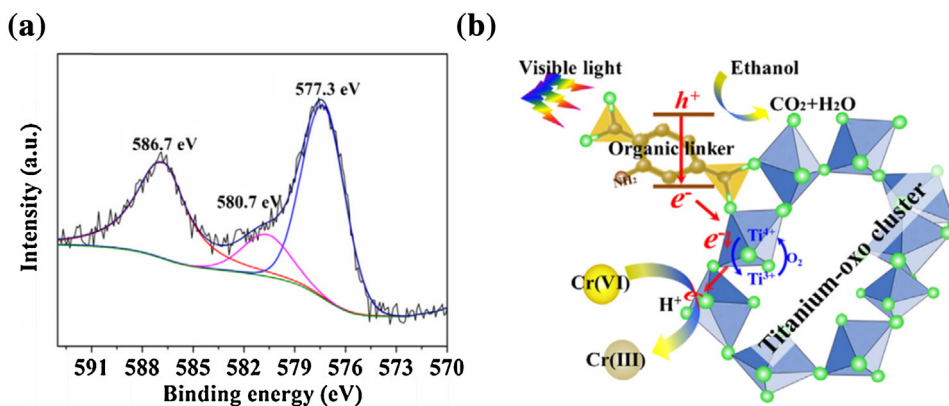


**Fig. 3.** (a) Cr 2p spectrum of NH<sub>2</sub>-MIL-125(Ti) after photocatalytic process; (b) schematic illustration of photocatalytic Cr(VI) reduction over NH<sub>2</sub>-MIL-125(Ti) under visible-light irradiation ( $\lambda > 420$  nm) [106], copyright (2015) Elsevier.

the surface of NH<sub>2</sub>-MIL-125(Ti) acts as hole scavengers to form CO<sub>2</sub> and H<sub>2</sub>O in this photocatalytic reaction system, and thus provides a basic environment for promoting the photocatalytic Cr(VI) reduction.

To test the reusability of the photocatalyst, NH<sub>2</sub>-MIL-125(Ti) has been investigated in successive runs after washing with HNO<sub>3</sub> and deionized water, and drying. There is only tiny decay (about 8%) in the photocatalytic activity after 5 runs of application, implying the reusability of NH<sub>2</sub>-MIL-125(Ti).

### 2.1.2. UiO-66(NH<sub>2</sub>)

Considering the high stability, adjustability and photo-responsiveness [129], UiO-66, a nano-size Zr-metal organic framework, was used to perform photocatalytic degradation of organic pollutants [130], CO<sub>2</sub> reduction [131], hydrogen generation [132]. Wu and co-workers reported the selective photocatalytic oxidation of alcohols to their corresponding aldehydes and photocatalytic reduction of Cr(VI) to Cr(III) over UiO-66(NH<sub>2</sub>), a derivative of UiO-66, under visible light [101]. The 2-aminoterephthalate (ATA) as organic linker in UiO-66(NH<sub>2</sub>) can act as an antenna to

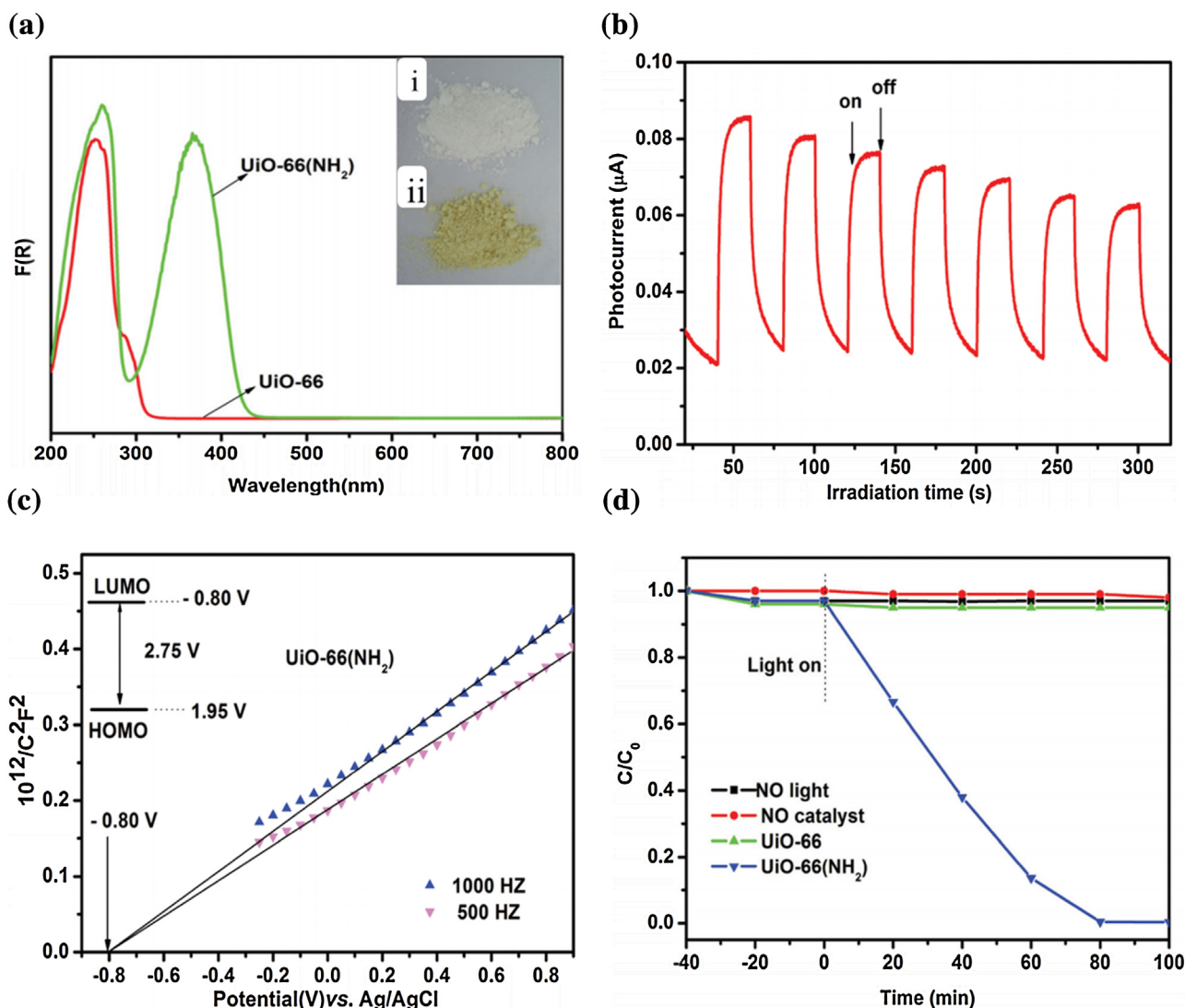
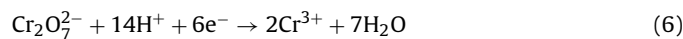
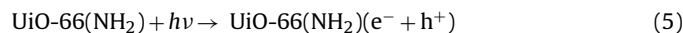


**Fig. 4.** (a) UV-vis spectra of UiO-66 and UiO-66(NH<sub>2</sub>); inset are the photographs of UiO-66 (i) and UiO-66(NH<sub>2</sub>) (ii); (b) transient photocurrent response of UiO-66(NH<sub>2</sub>) in 0.2 M Na<sub>2</sub>SO<sub>4</sub> aqueous solution without bias versus Ag/AgCl under the irradiation of visible light ( $\lambda \geq 420$  nm); (c) Mott-Schottky plot of UiO-66(NH<sub>2</sub>) in 0.2 M Na<sub>2</sub>SO<sub>4</sub> aqueous solution (pH = 6.8); (d) reaction profiles of photocatalytic reduction of Cr(VI). Reaction conditions: 20 mg photocatalyst, 40 mL of 10 ppm Cr(VI), 100  $\mu$ L methanol, reaction temperature 30 °C, pH = 2 [101], copyright (2013) Royal Society of Chemistry.

absorb visible light, resulting into that its photo-absorption edge was shifted to the visible region, which was confirmed by its color changing from white to yellow, as shown in Fig. 4(a). The result of transient photocurrent response of UiO-66(NH<sub>2</sub>) under intermittent visible light irradiation ( $\lambda \geq 420$  nm) exhibited that it can be photo-excited to form electron-hole pairs, and these photo-generated carriers can be immediately separated upon contact with a high work function conductor, as illustrated in Fig. 4(b). The Mott-Schottky-type plot of UiO-66(NH<sub>2</sub>) suggested that it is a typical n-type semiconductor, and its flat-band potential ( $V_{fb}$ ) at ca.  $-0.80$  V vs. Ag/AgCl is more negative than that of  $O_2^{\cdot-}/O_2$  ( $-0.28$  V) [133] and Cr(VI)/Cr(III) ( $+1.15$  V, pH = 3.0) [134] (Fig. 4(c)). Also, the calculated  $V_{CB}$  is reported as  $1.95$  V vs. Ag/AgCl. Based on these information, over the UiO-66(NH<sub>2</sub>), it is thermodynamically possible to transfer the photogenerated electrons onto the absorbed  $O_2$  and to form the superoxide radical species, which can potentially reduce Cr(VI) to Cr(III). The photocatalytic reduction of Cr(VI) to Cr(III) was carried out at 30 °C in a 100 mL quartz reactor containing 20 mg UiO-66 or UiO-66(NH<sub>2</sub>) and 40 mL 10 ppm Cr(VI) aqueous solution with the pH value being 2.0 and 100  $\mu$ L methanol as hole scavengers, following the Eqs. (5)–(7). As depicted in Fig. 4(d), UiO-

66(NH<sub>2</sub>) showed high reduction ratio of Cr(VI), which increased to 97% after 80 min visible light illumination. The stability of UiO-66(NH<sub>2</sub>), which was used for three runs, was confirmed by X-ray diffraction (XRD), FTIR, and XPS. The results revealed that no noticeable differences can be found for the original UiO-66(NH<sub>2</sub>) (Fresh) sample, the sample of UiO-66(NH<sub>2</sub>) (Used 1) after the oxidation process of alcohols and the UiO-66(NH<sub>2</sub>) (Used 2) after the Cr(VI) reduction reaction.



### 2.1.3. NH<sub>2</sub>-MIL-88B(Fe), NH<sub>2</sub>-MIL-53(Fe) and NH<sub>2</sub>-MIL-101(Fe)

The MIL-88B(Fe) is built up of Fe<sub>3</sub>- $\mu_3$ -oxo clusters linked by oxidation stable terephthalate (BDC) ligands, in which Fe<sub>3</sub>- $\mu_3$ -oxo cluster exhibits octahedral geometry with three Fe(III) atoms, four oxygen atoms from bidentate BDC, one  $\mu_3$ O oxygen atom and one oxygen atoms from terminal ligands like water molecules [135]. The amine-functionalized MIL-88B(Fe) (NH<sub>2</sub>-MIL-88B(Fe)) showed the identical PXRD patterns with MIL-88B, implying they possess

the same crystal phase structure. Mott-Schottky measurements were carried out to elucidate the semiconductor properties of MIL-88B and NH<sub>2</sub>-MIL-88B. The results revealed that their flat-band potential is ca. 0.13 V versus NHE, more negative than +1.15 V of Cr(VI)/Cr(III) at pH = 3.0 [112], demonstrating that both of them can be potentially used to conduct Cr(VI) reduction.

Under visible light irradiation, NH<sub>2</sub>-MIL-88B(Fe) exhibited better Cr(VI) reduction performance than MIL-88B(Fe), NH<sub>2</sub>-UiO-66-Zr, NH<sub>2</sub>-MIL-125-Ti, N-doped TiO<sub>2</sub>, g-C<sub>3</sub>N<sub>4</sub>, CdS and P25 at pH = 2.0, as illustrated in Fig. 5(a) and (b) [45]. NH<sub>2</sub>-MIL-88B(Fe) possessed excellent stability and reusability at pH range of 2.0–4.0 as photocatalyst, especially after experiencing recovery by filtration, washing with water and ethanol and drying under vacuum, which was confirmed by SEM, PXRD, FTIR and XPS. It was worthy to mentioning that a weak peak at 577.1 eV can be assigned to Cr 2p in Cr(OH)<sub>3</sub> form [112], which can further confirm the fact of Cr(VI) reduction to Cr(III) over NH<sub>2</sub>-MIL-88B(Fe).

Considering that MIL-88B(Fe) and NH<sub>2</sub>-MIL-88B(Fe) possess the identical photocatalytically active Fe<sub>3</sub>-μ<sub>3</sub>-oxo clusters and reduction potential of ca. 0.13 V versus NHE, the NH<sub>2</sub>-group from BDC-NH<sub>2</sub> can be appointed to enhance the photocatalytic performance of NH<sub>2</sub>-MIL-88B(Fe) due to improved ligand-to-metal charge transfer (LMCT) [123,136]. A dual excitation pathways mechanism was proposed to clarify the photocatalytic reduction of Cr(VI) to Cr(III) over NH<sub>2</sub>-MIL-88B(Fe), as illustrated in Fig. 5(d). Upon the visible light illumination, both NH<sub>2</sub>-BDC and Fe<sub>3</sub>-μ<sub>3</sub>-oxo clusters in NH<sub>2</sub>-MIL-88B(Fe) were excited. The electrons from the excited Fe<sub>3</sub>-μ<sub>3</sub>-oxo clusters as well as the photogenerated electrons transferred from NH<sub>2</sub>-BDC to Fe<sub>3</sub>-μ<sub>3</sub>-oxo clusters can achieve Cr(VI) reduction to Cr(III), which was confirmed by photoluminescence (PL), electron spin resonance (ESR), and transient photocurrent [123,136,137].

Three iron(III)-based MOFs like MIL-88B(Fe), MIL-53(Fe) and MIL-101(Fe) were selected to investigate the influences resulted from the amine functionality on photocatalytic activities for Cr(VI) reduction. As shown in Fig. 5(c) amine-functionalized ones exhibited higher visible light absorption and stronger photocatalytic activities than unfunctionalized ones, implying that amine-functionalization of iron(III)-based MOFs is a flexible way to increase the photocatalytic activities on Cr(VI) reduction. However, being compared to unfunctionalized MIL-88B(Fe), MIL-53(Fe) and MIL-101(Fe), the performance enhancements for Cr(VI) of their corresponding amine-functionalized ones are quite different, which can be ascribed to their distinct structure and electron transfer efficiency.

## 2.2. Semiconductor/MOFs hybrid photocatalysts

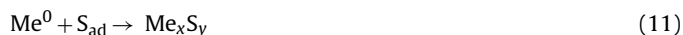
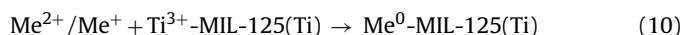
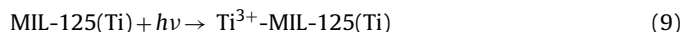
In recent years, the photocatalytic Cr(VI) reduction over visible-light active photocatalysts like CdS had been widely reported [18,22,23,26,42,138–140]. However, the efficiency of these photocatalysts for Cr(VI) reduction is not high enough and the reduction rate is usually slow. Thus, some heterostructures consisting of narrow gap semiconductors and MOFs are highly expected as highly visible-light-active photocatalysts [126,141]. This strategy can be extended for tuning the photocatalytic performance of many MOFs and pave a novel way to fabricate semiconductor/MOFs heterogeneous catalyst for solar-chemical energy conversion applications.

### 2.2.1. Me<sub>x</sub>S<sub>y</sub> @ MIL-125(Ti) (Me<sub>x</sub>S<sub>y</sub> = CdS, In<sub>2</sub>S<sub>3</sub>, SnS<sub>2</sub>, Sb<sub>2</sub>S<sub>3</sub>)

Beside the amine-fictionalization, another strategy to tune the photo-excited light of MIL-125(Ti) from UV light region to visible light region is the introduction of metal sulfides (simply expressed as Me<sub>x</sub>S<sub>y</sub>), like CdS, In<sub>2</sub>S<sub>3</sub>, SnS<sub>2</sub>, Sb<sub>2</sub>S<sub>3</sub>, etc, which had been identified as visible photocatalysts owing their narrow energy band gaps, and had been widely used to carry out photocatalytic

degradation of organic pollutants in aqueous solution [142–147]. Yuan and co-workers developed a facile *in situ* photodeposition method to achieve the composites of Me<sub>x</sub>S<sub>y</sub> (CdS, In<sub>2</sub>S<sub>3</sub>, SnS<sub>2</sub>, Sb<sub>2</sub>S<sub>3</sub>) into MIL-125(Ti) for the first time [126]. The XRD patterns of the as-prepared composites exhibited high crystallizations and no noticeable changes from MIL-125(Ti), implying the phase structure of parent MIL-125(Ti) remains intact after the photodeposition of Me<sub>x</sub>S<sub>y</sub>, as illustrated in Fig. 6(a). TEM and HRTEM were used to gain further insight of the microstructure of the composites, as shown in Fig. 6(b)–(e), in which the sizes of Ag<sub>2</sub>S, CdS and CuS quantum dots (QDs) dispersed onto MIL-125(Ti) are within 10 nm. Two parallel lattice fringes could be found in the HRTEM images of the composites, of which the nearest distances are well agreement with the values for the [220], [101] and [101] planes of Ag<sub>2</sub>S, CdS and CuS, respectively. While, as depicted in Fig. 6(f), the MoS<sub>2</sub> particles were layered onto MIL-125(Ti) surface with a large contact area, in which the lattice fringes with nearest distance of 0.583 nm matched well with the value for the [002] plane of hexagonal MoS<sub>2</sub>. The deposition of Me<sub>x</sub>S<sub>y</sub> QDs onto MIL-125(Ti) was further confirmed by XPS measurement. Compared to the XPS spectrum of pure MIL-125(Ti), some new peaks at 367.8, 405.3, 932.6 and 231.9 eV could be assigned to Ag 3d, Cd 3d, Cu 2p and Mo 3d, respectively, as well as the new peaks in the range of 161.1–169.1 eV were indicative the presence of S components.

A possible mechanism of photodeposition of Me<sub>x</sub>S<sub>y</sub> QDs onto MIL-125(Ti) was also proposed, as shown in Fig. 7(c). The large surface area and pore structure of MIL-125(Ti) enhanced the adsorption of metal ions like Cd<sup>2+</sup>, Cu<sup>2+</sup>, Ag<sup>+</sup> and MoS<sub>4</sub><sup>2−</sup>. Under the UV light irradiation, Ti<sup>4+</sup> ions in original MIL-125(Ti) were transformed into Ti<sup>3+</sup> ions with strong reducing ability (−1.37 V vs SHE), which quickly reduced the metal precursors (Cd<sup>2+</sup>, Cu<sup>2+</sup>, Ag<sup>+</sup> and MoS<sub>4</sub><sup>2−</sup>) into Me<sup>0</sup> (Me = Cd, Cu, Ag and Mo). The reaction between Me<sup>0</sup> and S<sub>8</sub> produced the corresponding metal sulfides as outlined in Eqs. (8)–(11).



The introduction of Me<sub>x</sub>S<sub>y</sub> QDs into MIL-125(Ti) can extend the light absorption from UV to visible region, and decrease the surface area and pore volume (as listed in Table 2) due to the surface block of cavities in MIL-125(Ti) by the Me<sub>x</sub>S<sub>y</sub> QDs. Due to that the photosensitizing effect and the enhanced light harvesting efficiency in the visible light area are achieved by simply introducing the narrow-band Me<sub>x</sub>S<sub>y</sub> QDs semiconductor, Ag<sub>2</sub>S/MIL-125(Ti), CdS/MIL-125(Ti), CuS/MIL-125(Ti) and MoS<sub>2</sub>/MIL-125(Ti) exhibited higher photocatalytic efficiency on Cr(VI) reduction than pure MIL-125(Ti), which can be evidenced from the photocatalytic reduction rate constants (*k*) of 0.0101 (CuS/MIL-125(Ti)), 0.0060 (MoS<sub>2</sub>/MIL-125(Ti)), 0.0058 (CdS/MIL-125(Ti)) and 0.0035 min<sup>−1</sup> (Ag<sub>2</sub>S/MIL-125(Ti)), as illustrated in Fig. 7(a) and (b).

Considering the characterizations and experiment data, a mechanism to clarify the photocatalytic Cr(VI) reduction in Me<sub>x</sub>S<sub>y</sub>@MIL-125(Ti) can be expressed as illustrated in Fig. 7(d). Upon the visible light irradiation, the excited state electrons on the conduction band (CB) of Me<sub>x</sub>S<sub>y</sub> can be transferred to MIL-125(Ti), while the holes of the valence band (VB) can be captured by ethanol, which was further mineralized into CO<sub>2</sub> and H<sub>2</sub>O. Finally, the electrons accumulated on the MIL-125(Ti) reduce Cr(VI) to Cr(III) under the acid condition following Eq. (12). The introduction of Me<sub>x</sub>S<sub>y</sub> as cocatalysts into MIL-125(Ti) can not only produce more active sites under visible light irradiation, but also create a heterojunction to accelerate the photoinduced electron–hole charge separation

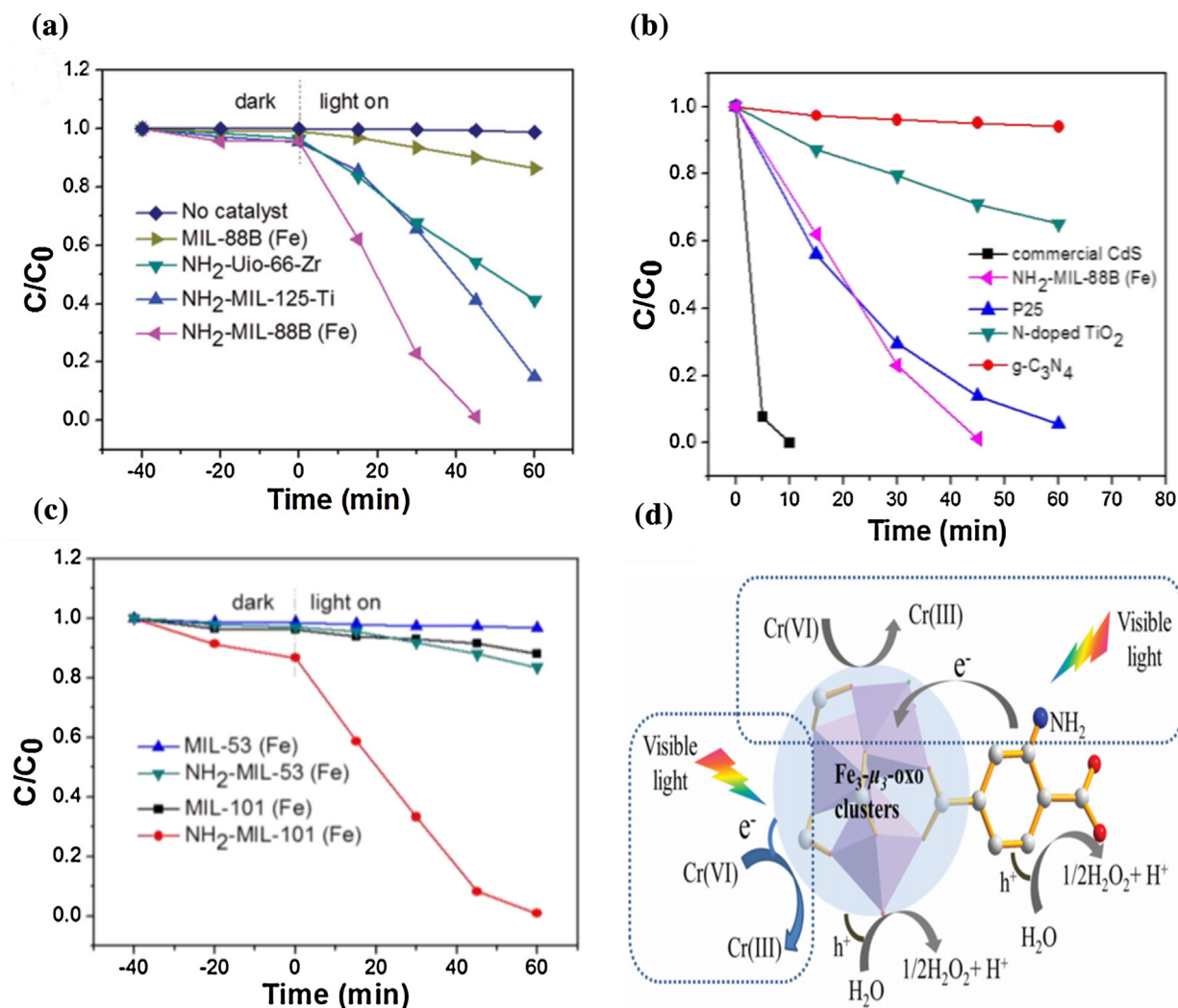


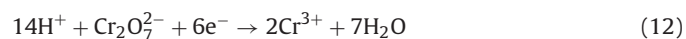
**Fig. 5.** (a) Reduction profiles of photocatalytic reduction of Cr(VI) under visible light irradiation over MIL-88B(Fe), NH<sub>2</sub>-Uio-66-Zr, NH<sub>2</sub>-MIL-125-Ti, NH<sub>2</sub>-MIL-88B(Fe), respectively. (b) Reduction profiles of photocatalytic reduction of Cr(VI) over NH<sub>2</sub>-MIL-88B(Fe), N-doped TiO<sub>2</sub>, g-C<sub>3</sub>N<sub>4</sub>, commercial CdS and P25, respectively. The solution is stirred for 40 min in the dark and then is exposed to visible light irradiation. (c) Reduction profiles of photocatalytic reduction of Cr(VI) over MIL-101(Fe), NH<sub>2</sub>-MIL-101(Fe), MIL-53(Fe) and NH<sub>2</sub>-MIL-53(Fe). Reaction condition: 20 mg photocatalyst, 40 mL of 8 ppm Cr(VI), reaction temperature is 30 °C, pH = 2. P25 is conducted in UV-vis light and the other photocatalysts are conducted in visible light. (d) Proposed dual excitation pathways mechanism for photocatalytic reduction of Cr(VI) over NH<sub>2</sub>-MIL-88B(Fe) [45], copyright (2015) John Wiley and Sons.

**Table 2**

The Brunauer–Emmer–Teller surface area ( $S_{\text{BET}}$ ) and total pore volume of MIL-125(Ti) and metal sulfides/MIL-125(Ti) composites [126].

Compounds	MIL-125(Ti)	Ag <sub>2</sub> S/MIL-125(Ti)	CdS/MIL-125(Ti)	CuS/MIL-125(Ti)	MoS <sub>2</sub> /MIL-125(Ti)
$S_{\text{BET}}$ (m <sup>2</sup> g <sup>-1</sup> )	1548.3	1023.3	1028.8	1402.7	1376.1
Total pore volume (cm <sup>3</sup> g <sup>-1</sup> )	0.758	0.686	0.626	0.693	0.672

rate and weak the possibility of charge recombination, finally to enhance the photocatalytic reduction of Cr(VI).



### 2.2.2. ZnO@ZIF-8

Zeolitic imidazolate framework-8 (ZIF-8) constructed from imidazolate (Hmim) organic ligands and Zn<sup>2+</sup> centre ions, exhibits high thermal and chemical stability [148]. Considering its high BET specific surface area and permanent porosity [148], ZIF-8 has been reported for gas storage [149,150], gas separation [151,152], catalysis [153,154], photocatalysis [66] and sensing [155]. On the other hand, ZnO with a band gap of 3.3 eV is often used as typical semiconductor photocatalyst to conduct organic pollutants degradation [156–158] and Cr(VI) reduction [18]. Wang and co-

workers reported that ZnO@ZIF-8 core-shell heterostructures were prepared via in-situ ZIF-8 crystal growth on ZnO colloidal spheres, which were further utilized to perform selective photoreduction of Cr(VI) from mixed Cr(VI)/MB solution [110]. The presences of ZnO and ZIF-8 in ZnO@ZIF-8 were confirmed by both PXRD (Fig. 8(a)) and FTIR, in which ZnO exhibited colloidal spheres with uniform size of 200–300 nm (Fig. 8(b) and (c)). And its inner structure was investigated by TEM, revealing that the ZIF-8 crystal polyhedrons were covered by ZnO colloids with thickness of ca. 30 nm, as shown in Fig. 8(d).

The fabrication of ZnO@ZIF-8 core-shell heterostructures was heavily influenced by the Hmim concentration in methanol and reaction time. As listed in Table 3 and Fig. 9(a)–(e), in the case of Hmim concentration being 3.66 M, the high Rc/Rr (Rc is Zn<sup>2+</sup> release



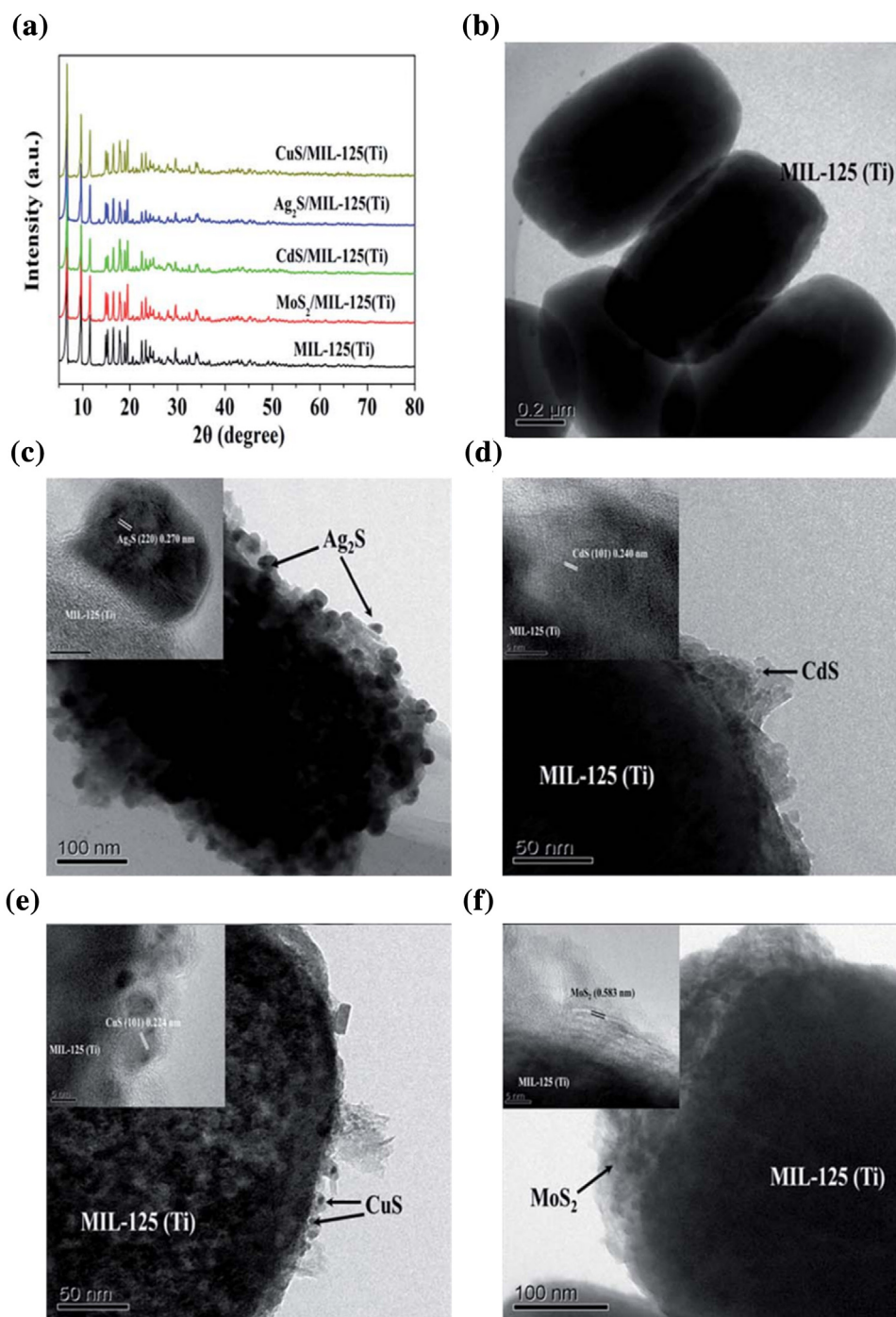


**Fig. 6.** (a) XRD patterns, TEM images and the corresponding HRTEM images of (b) pure MIL-125(Ti), (c)  $\text{Ag}_2\text{S}/\text{MIL-125(Ti)}$ , (d)  $\text{CdS}/\text{MIL-125(Ti)}$ , (e)  $\text{CuS}/\text{MIL-125(Ti)}$  and (f)  $\text{MoS}_2/\text{MIL-125(Ti)}$  [126], copyright (2015) Royal Society of Chemistry.

**Table 3**

Dependence of pH,  $I_{\text{ZIF-8}}$ ,  $I_{\text{ZnO}}$  and structure on concentration of Hmim [110].

Concentration of Hmim (M)	pH	$I_{\text{ZIF-8}}/(I_{\text{ZIF-8}} + I_{\text{ZnO}})$	Structure
4.51	10.69	0.6	Core-shell and polyhedrons
3.66	10.54	0.53	Core-shell
1.83	10.22	0.88	Polyhedrons and ZnO
0.915	9.81	0.35	Core-shell and polyhedrons
0.366	9.42	0.21	Core-shell and polyhedrons

Note:  $I_{\text{ZIF-8}}$  and  $I_{\text{ZnO}}$  refer to intensity of XRD peak located at  $7.42^\circ$  [(001) plane of ZIF-8] and  $36.16^\circ$  [(101) plane of ZnO] (Fig. 9), respectively.

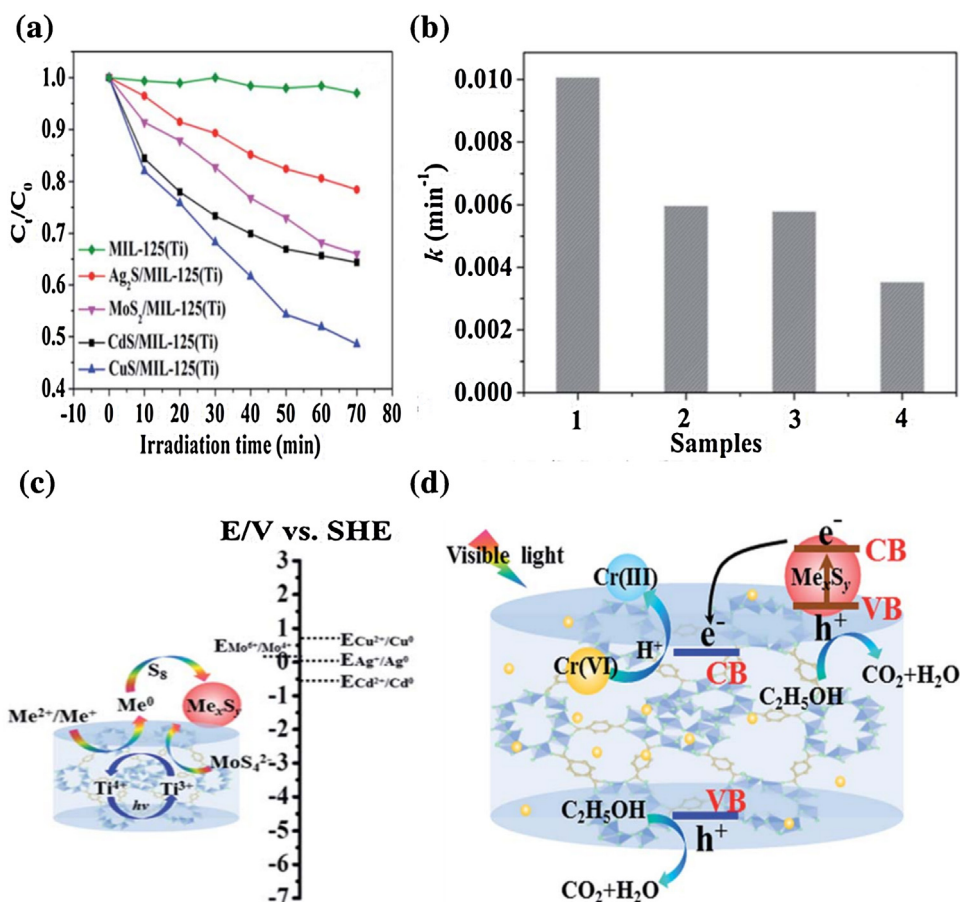


**Fig. 7.** (a) Photocatalytic activities of the obtained samples for the reduction of Cr(VI) under the visible light irradiation. (b) The rate constant  $k$  of (1) CuS/MIL-125(Ti), (2)  $MoS_2/MIL-125(Ti)$ , (3)  $CdS/MIL-125(Ti)$  and (4)  $Ag_2S/MIL-125(Ti)$ ; (c) schematic representation of the mechanisms of the MexSy photodeposition on MIL-125(Ti); (d) schematic illustration of photocatalytic Cr(VI) reduction over  $Me_xS_y/MIL-125(Ti)$  under visible-light irradiation ( $\lambda > 420$  nm) [126], copyright (2015) Royal Society of Chemistry.

rate, and  $R_c$  is coordination rate between  $Zn^{2+}$  and Hmim) ratio resulted in the formation of ZnO@ZIF-8 core-shell heterostructure with shell thickness of ca. 30 nm, as I zone illustrated in Fig. 9(f). The  $R_c/R_r$  decline resulting from the decrease of Hmim concentration to 1.83 M leads to the fabrication of ZIF-8 polyhedrons as III zone shown in Fig. 9(f). While the increase of Hmim concentration to 4.51 and 4.0 M or the decrease of Hmim concentration to 3.0, 0.915 and even 0.366 M brings out both ZnO@ZIF-8 core-shell and ZIF-8 polyhedron, as II zone depicted in Fig. 9(f). The time-dependent experiment revealed that reaction time of 8 min can cause ZnO sphere being totally covered with ZIF-8 polyhedrons to form ZnO@ZIF-8 core-shell. Also, the formation mechanism of ZnO@ZIF-8 core-shell was investigated. Considering that ZnO can be dissolved in basic or acidic solutions [99],  $Zn^{2+}$  ions will be release from ZnO colloids in Hmim methanol solution with pKa being 14.2 [159,160]. The release rate of  $Zn^{2+}$  is subject to the Hmim concentration with different pH values (Table 3), and high mol ratio of Hmim/ $Zn^{2+}$  might increase the nucleation rate of ZIF-8 [160,161]. When Hmim concentration is 3.66 M, the integrated ZnO@ZIF-8 core-shell heterostructures can be fabricated as illustrated in Fig. 9(f). As Hmim concentration is fixed to 1.83 M, the substantially decreased coordination rate between  $Zn^{2+}$  and Hmim cannot achieve wrap of ZIF-8 over ZnO. The mixture of ZnO@ZIF-8 core-shell heterostructures and ZIF-8 polyhedrons was obtained at other Hmim concentration. In other word, ZnO@ZIF-8 core-shell heterostructures can be harvested via the adjust of Hmim concentration. The proposed formation mechanism was confirmed by XRD, SEM and TEM.

Compared with ZnO colloidal spheres, the absorption edge of ZnO@ZIF-8 core-shell heterostructures exhibits minor red-shift. The band gap of ZnO@ZIF-8 (3.24 eV) is slightly smaller than that of ZnO (3.27 eV), which can be contributed to the heterostructural effect after the introduction of ZIF-8 [162]. The photocatalytic performances of ZnO@ZIF-8 and ZnO were investigated via the treatment of mono-composition aqueous solution or two-component mixed solution of MB and Cr(VI). During the photocatalysis procedure, ZnO can produce electrons and holes upon UV light illumination to conduct both Cr(VI) reduction and organic pollutants degradation [163]. As illustrated in Fig. 10(a), ZnO@ZIF-8 exhibits higher photocatalytic Cr(VI) reduction performance than that of ZnO. And its achievement in mixed MB and Cr(VI) aqueous solution (the corresponding efficiency being nearly 100% after 70 min irradiation) is better than that in individual Cr(VI) solution (with ca. 50% efficiency after 80 min irradiation).

It is worthy to noting that ZnO@ZIF-8 prefers to reduce Cr(VI) into Cr(III) in the mixed solution of MB and Cr(VI), which can be assigned to adsorption and size selectivity of ZIF-8 shell towards Cr(VI) ions. It is generally deemed that ZIF-8 is positive in acidic or neutral conditions [66,164], and  $CrO_4^{2-}$  is the main species of Cr(VI) at pH being ca. 7.0 [165]. The anionic Cr(VI), not cationic MB, prefers to be absorbed to ZIF-8 shell via electrostatic interaction, which was confirmed by the zeta potential of ZnO@ZIF-8 heterostructures from ca. +25 mV at pH = 5.0 to -35 mV at pH = 12.0 with positive charge at pH range of 5.0–10.0.

According to the previous report,  $CrO_4^{2-}$  ions with ionic diameter of 4 Å can penetrate into the channel (ca. 3.4 Å) of ZIF-8

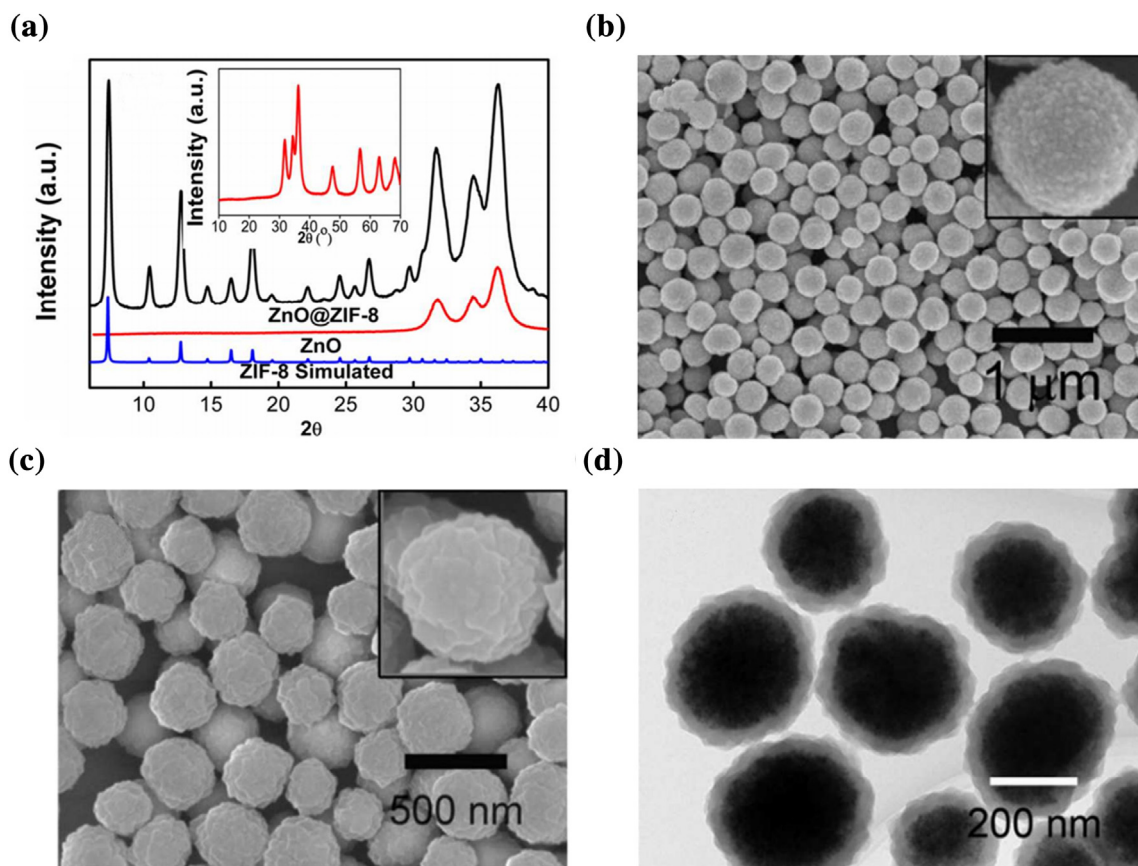


**Fig. 8.** (a) XRD patterns of as-prepared ZnO colloidal spheres and ZnO@ZIF-8 heterostructures. Inset is the whole XRD pattern of ZnO colloidal spheres from 10° to 70°; (b) SEM images of ZnO colloidal spheres; (c) SEM images of ZnO@ZIF-8 heterostructures; (d) TEM image of ZnO@ZIF-8 heterostructures [110], copyright (2016) American Chemical Society.

frameworks [166,167], while MB with minimum cross-section size of 8 Å cannot enter the apertures of ZIF-8 [168]. Therefore, besides the adsorption selectivity, size selectivity of ZIF-8 shell plays a crucial role in enhancing the selectivity of photocatalysis process to Cr(VI) and MB, which was further confirmed by the introduction of RhB (molecular size of 15.9 × 11.8 × 5.6 Å).

### 2.3. Conductor/MOFs hybrid photocatalysts

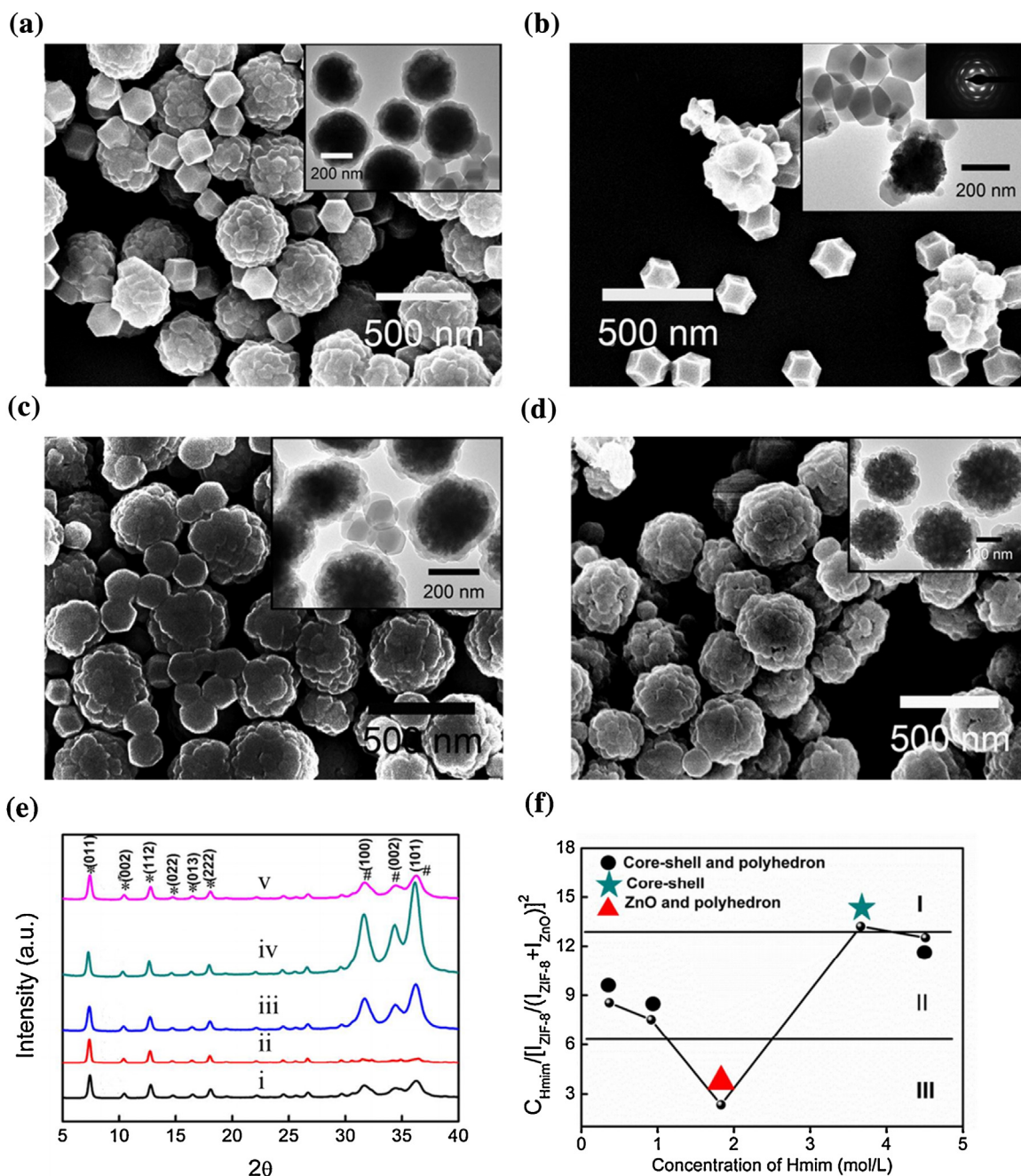
Noble metal nanoparticles (NPs) with controllable size distribution have received enormous attentions due to their unique properties and potential applications like catalysis. Their catalytic performances are highly dependent on the dispersion of active metal sites. In order to avoid their aggregation during the synthesis, some porous materials have been designed to stabilize these noble metal NPs [169]. As a new class of porous materials with high porosity and large surface area, MOFs can be selected to control the growth of NPs in the confined cavities and to produce highly dispersed NPs, which can significantly improve their catalytic performance. While, graphene with superior physicochemical properties has been regarded as an important component for making various functional composite materials [170,171]. The introduction of GO into MOFs is expected to enhance the MOFs' photocatalytic behavior due to that GO can slow the recombination of photogenerated electron-hole pairs and increase the electron charge transfer rate [172]. It would provide useful insight to design and fabricate conductor-MOFs hybrids, which can be used to conduct photocatalytic reaction like Cr(VI) reduction.

#### 2.3.1. Pd@UiO-66(NH<sub>2</sub>)

In order to further enhance the photocatalytic performance of UiO-66(NH<sub>2</sub>), highly dispersed Pd nanoparticles (NPs) of about 3–6 nm in diameter (as illustrated in Fig. 11(a)) are immobilized into via a facile one-pot hydrothermal method [112]. The X-ray diffraction patterns of the as-prepared UiO-66(NH<sub>2</sub>) and Pd@UiO-66(NH<sub>2</sub>) nanocomposites are identical, demonstrating excellent crystallinity of the samples. In the XRD patterns, no characteristic diffractions of metallic Pd can be found, probably due to the relatively low content of Pd in the as-prepared Pd@UiO-66(NH<sub>2</sub>) (0.93 wt% determined by ICP) and tiny particle size Pd NPs being distributed on the UiO-66(NH<sub>2</sub>) surface uniformly. The hydrothermal processing did not destroy the integrity of characteristic structure of UiO-66(NH<sub>2</sub>) in Pd@UiO-66(NH<sub>2</sub>) composite, in which Pd NPs were homogeneously dispersed over the UiO-66(NH<sub>2</sub>), as illustrated in Fig. 11(b) and (c). The Pd NPs were stable in composite, and no leaching of Pd occurred even after washing and sonication. From the HRTEM image, it could be found that Pd nanoparticles were encapsulated within the pores of UiO-66(NH<sub>2</sub>) with vague distorted lattice fringes, while most of the larger Pd NPs disperse on the surface of the UiO-66(NH<sub>2</sub>) have clear lattice fringes, as shown in Fig. 11(d). The XPS survey spectrum confirmed the existence of Zr, Pd, O, N and C in the composite. The weak signal of Pd is due to the relatively low content of Pd in the nanocomposite.

From the UV–vis diffuse reflectance spectra, it could be found that the introduction of Pd nanoparticles enhanced the light absorption intensity of the UiO-66(NH<sub>2</sub>) in the visible light region, which can be further be confirmed by the color change from pale yellow to brown. Compared with the UiO-66(NH<sub>2</sub>), the photocurrent over Pd@UiO-66(NH<sub>2</sub>) was enhanced, as shown in





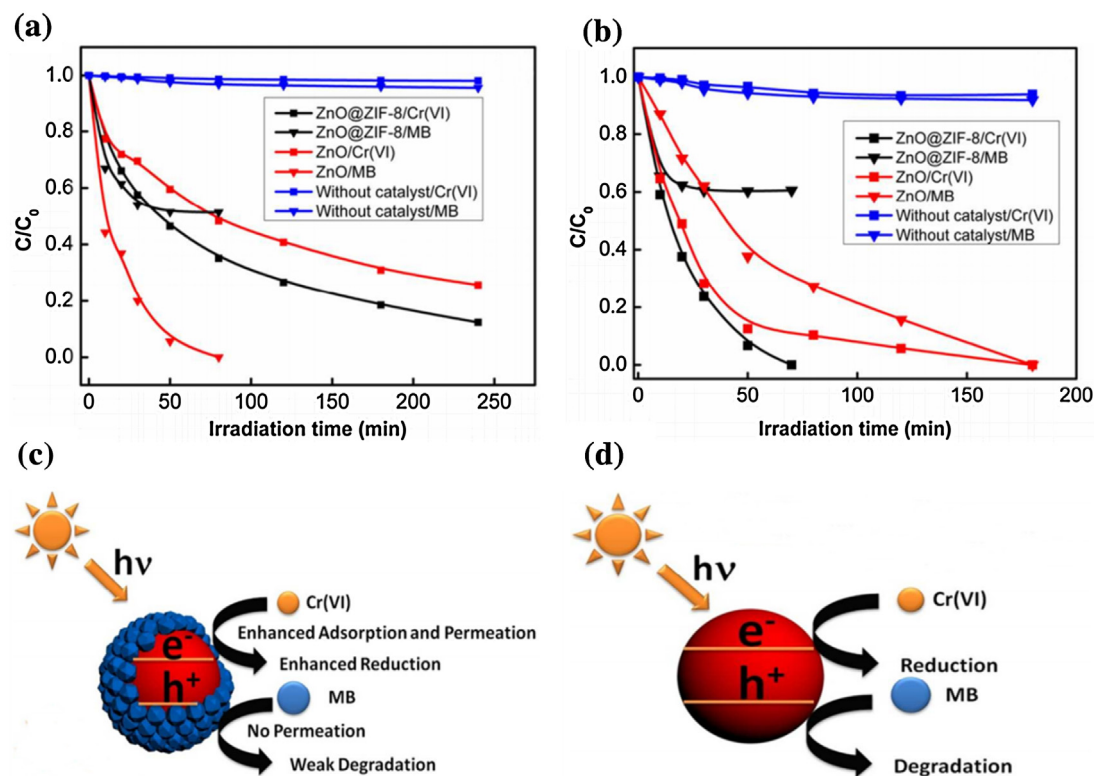
**Fig. 9.** SEM and TEM (inset) images of products obtained with different concentration of Hmim (a) 4.51 M, (b) 1.83 M [inset: selected area electron diffraction (SAED) pattern of the colloidal sphere in TEM image] (c) 0.915 M and (d) 0.366 M. (e) XRD patterns of the product obtained with different Hmim concentration (i) 4.51 M, (ii) 1.83 M, (iii) 0.915 M, (iv) 0.366 M and (v) 3.66 M. (f) Structure dependence of the obtained product on Hmim concentration. Note: ZIF-8 peaks were labeled as “#” [110], copyright (2016) American Chemical Society.

Fig. 12(a), indicating that the separation efficiency of photoexcited electron–hole pairs and the lifetime of the photogenerated charge carriers are improved through the interaction between Pd and UiO-66(NH<sub>2</sub>), which was confirmed by both transient photocurrent responses and photoluminescence measurements, as illustrated in Fig. 12(b). The introduction of Pd NPs led to slight increase of BET surface area from 756.04 m<sup>2</sup> g<sup>−1</sup> for UiO-66(NH<sub>2</sub>) to 836.6 m<sup>2</sup> g<sup>−1</sup> for Pd@UiO-66(NH<sub>2</sub>). It can be assumed that the remaining organic solvent molecules within the pores of UiO-66(NH<sub>2</sub>) had been thoroughly removed during the hydrothermal process, and most of the Pd NPs are finely dispersed on the surface rather than the pores of UiO-66(NH<sub>2</sub>) as confirmed by TEM (Fig. 11(b) and (c)). Furthermore, the pore size distribution curves exhibited that both

Pd@UiO-66(NH<sub>2</sub>) and UiO-66(NH<sub>2</sub>) were mainly composed of large size micropores. The greater specific surface area of the photocatalyst can contribute more surface active sites and enhance the transportation of the charge carriers, which finally improved the photocatalytic performance.

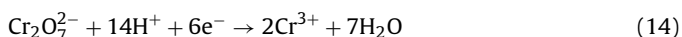
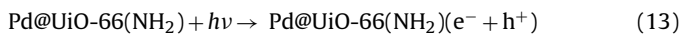
The enhanced absorption of visible light is expected to improve the photocatalytic performance of Pd@UiO-66(NH<sub>2</sub>) toward the Cr(VI) reduction. As depicted in Fig. 12(c), Pd@UiO-66(NH<sub>2</sub>) was active to photocatalytically reduce the Cr(VI) into Cr(III) with the reduction ratio of 99% upon visible light illumination ( $\lambda = 420$  nm) for 90 min. The high activity of Pd@UiO-66(NH<sub>2</sub>) can be ascribed to the intimate interfacial contact between Pd and UiO-66(NH<sub>2</sub>), which can facilitate the efficient charge separation. The Cr<sub>2</sub>O<sub>7</sub><sup>2−</sup>





**Fig. 10.** Photocatalytic removal curves of Cr(VI) and MB in the presence of ZnO@ZIF-8 heterostructures or ZnO spheres in (a) mono-component aqueous solutions and (b) two-component mixed Cr(VI) and MB aqueous solutions under UV irradiation. (c) Schematic illustration of selectively enhanced photocatalysis properties of the ZnO@ZIF-8 core-shell heterostructures. (d) Schematic illustration of photocatalysis properties of the ZnO [110], copyright (2016) American Chemical Society.

ions are the predominating species of chromium as pH being 2.0–6.0, and the possible main processes can be described as Eqs. (13)–(15).



Two typical organic dyes, namely methyl orange (MO) and methylene blue (MB), were mixed with Cr(VI) to perform further investigation on the photocatalytic performance of Pd@UiO-66(NH<sub>2</sub>), especially for eliminating different pollutants simultaneously. When the organic dyes (MB or MO) were added into the reaction system, the Cr(VI) reduction was significantly enhanced. In the binary systems of Cr(VI)/MO and Cr(VI)/MB, the Cr(VI) reduction rates Cr(VI) are 79% and 100% after 60 min of continuous visible light irradiation ( $\lambda = 420$  nm), respectively, which were obviously higher than that in the single Cr(VI) system (70%), as illustrated in Fig. 12(d). The presence of Cr(VI) can also increase the photocatalytic MB and MO degradation due to the synergic effect, as the process of photocatalytic oxidation of dye and reduction of Cr(VI) could consume photogenerated electrons and holes respectively, avoiding the recombination of photoexcited electron-hole pairs. It could be concluded that the enhanced photocatalytic performance of the Pd@UiO-66(NH<sub>2</sub>) nanocomposite toward photocatalytic degradation of aqueous Cr(VI) and organic dyes under visible light irradiation can be ascribed to the integrative factors of its enhanced light absorption intensity, prolonged lifetime of photogenerated charge carriers and increased BET surface area.

Finally, Wu and co-workers proposed a possible mechanism for the reduction of Cr(VI) and degradation of the organic dyes over Pd@UiO-66(NH<sub>2</sub>), as shown in Fig. 12(e). The zirconium-oxygen clusters within UiO-66(NH<sub>2</sub>) behaved as quantum dots, and the

–NH<sub>2</sub> groups in the ligand acted as auxochromic group to efficiently transfer the energy to the inorganic zirconium-oxygen clusters part as depicted in Fig. 13(f), which was further enhanced by the introduction of Pd NPs. Upon visible light irradiation, the charge carriers will be produced, and the photogenerated electrons and holes can be separately transferred to the surface of the photocatalyst quickly to participate in the Cr(VI) reduction and dyes degradation reactions. Wu and co-workers also reported that Fe-benzenedicarboxylate (MIL-53(Fe)) and MIL-53(Fe)-reduced graphene oxide could act as bifunctional photocatalyst to conduct photocatalytic oxidation of organic dyes (MG or RhB) and reduction of Cr(VI) [109,113].

### 2.3.2. RGO-UiO-66(NH<sub>2</sub>)

Considering that positive charge of UiO-66(NH<sub>2</sub>) due to the introduction of the amino (–NH<sub>2</sub>) group and the negatively charged surface of reduced graphene oxide (RGO) resulted from the deprotonation of the carboxyl groups during the dialysis process of GO, RGO-UiO-66(NH<sub>2</sub>) nanocomposites (NCs) could be easily assembled after hydrothermal reduction process [111]. The parent UiO-66(NH<sub>2</sub>) and RGO-UiO-66(NH<sub>2</sub>) possesses identical XRD patterns (Fig. 13(a)), which can be explained by two possible reasons: (1) the relatively low diffraction intensity of RGO at 26.0° may be shielded by one peak of UiO-66(NH<sub>2</sub>), and (2) the disappearance of the layer-stacking regularity after redox of graphite [173,174]. Also, no typical diffraction peak of GO at ca. 10.8° was observed, implying that the GO had been successfully reduced to RGO through the hydrothermal process, which was further confirmed from the XPS results. TEM and HRTEM images RGO-UiO-66(NH<sub>2</sub>) indicated that the characteristic structure of UiO-66(NH<sub>2</sub>) was retained, in which some UiO-66(NH<sub>2</sub>) were wrapped by RGO transparent thin 2D sheets via adequate interfacial interaction, as illustrated in Fig. 13(b). The successful incorporation of RGO into UiO-66(NH<sub>2</sub>)

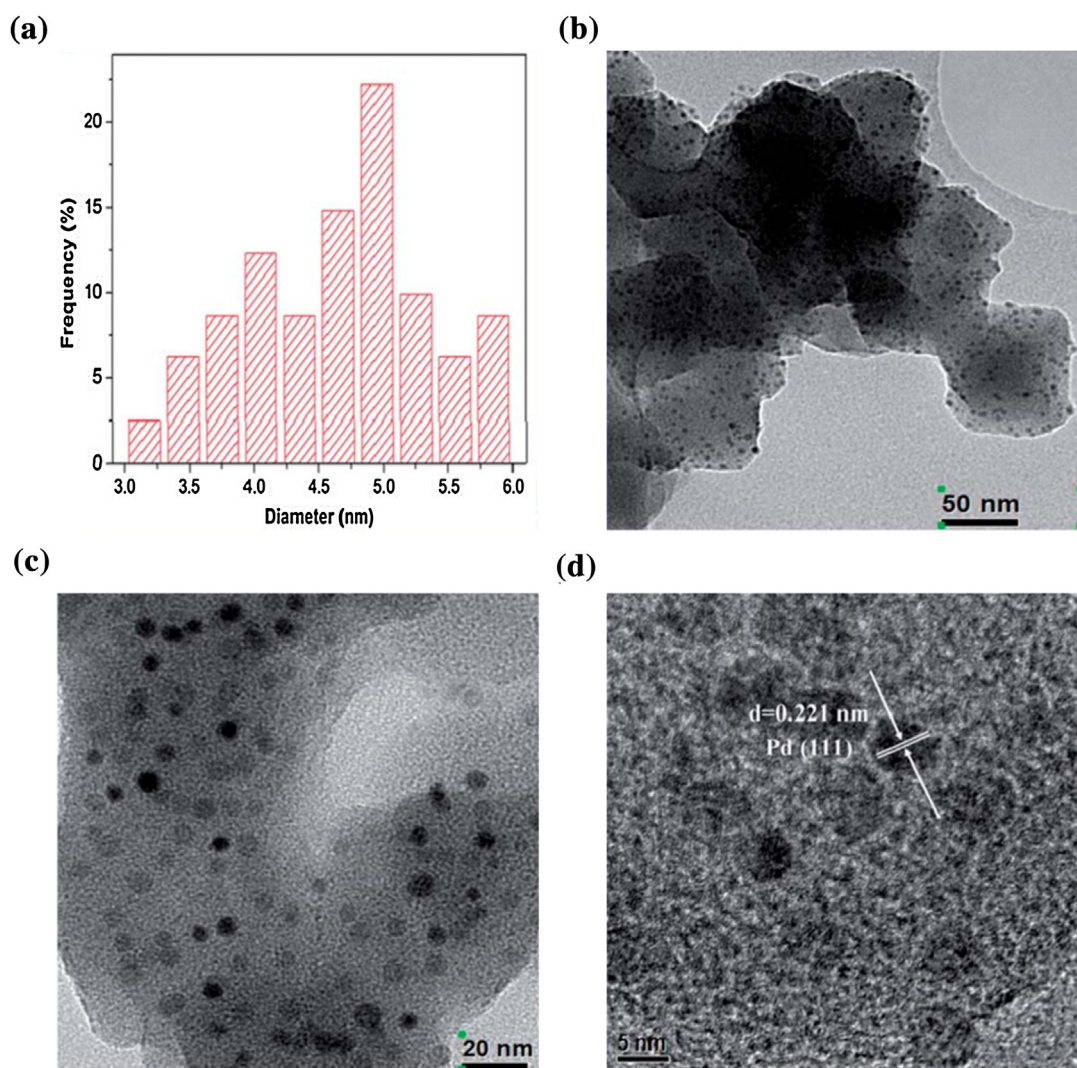


**Fig. 11.** (a) and (b) Results of TEM images for the Pd@UiO-66(NH<sub>2</sub>); (c) HRTEM image; and (d) corresponding size distribution of Pd nanoparticles [112], copyright (2013) Royal Society of Chemistry.

can be contributed to the electrostatic assembly via a relatively adequate interfacial interactions.

The UV–vis DRS revealed that an intense absorption band ranging from 300 to 450 nm can be found for UiO-66(NH<sub>2</sub>), in which a peak at 360 nm can be assigned to the presence of the amino group. While, a broad background adsorption in the visible-light region (450–800 nm) can be observed for RGO-UiO-66(NH<sub>2</sub>), implying the introduction of RGO into UiO-66(NH<sub>2</sub>) can enhance the visible light absorption intensity. The electrochemical analysis on UiO-66(NH<sub>2</sub>) and RGO-UiO-66(NH<sub>2</sub>) exhibited typical on-off cycles of intermittent visible light irradiation, as depicted in Fig. 13(c). The incorporation of RGO could increase the photocurrent greatly, implying that more efficient depart of photoexcited electron–hole pairs and longer lifetime of the photogenerated charge carriers can be achieved, which can be confirmed by the photoluminescence (PL) determination, as shown in Fig. 13(d). The introduction of RGO also led to the slight increase of BET surface area from 732.21 for parent UiO-66(NH<sub>2</sub>) to 766.54 m<sup>2</sup>g<sup>−1</sup> for 2% RGO-UiO-66(NH<sub>2</sub>). The BET surface area of RGO-UiO-66(NH<sub>2</sub>) increases with the RGO content (Table 4), as it could be assumed that the new pores were created at the interface between the UiO-66(NH<sub>2</sub>) and RGO [175]. In all, the enhanced light absorption intensity, longer lifetime of electron–hole pairs and larger specific surface area resulted from

the introduction of RGO into UiO-66(NH<sub>2</sub>) can be expected to significantly enhance its photocatalytic performance.

Therefore, the photocatalytic activities of Cr(VI) reduction over the as-prepared RGO-UiO-66(NH<sub>2</sub>) with different RGO contents under visible-light irradiation ( $\lambda = 420$  nm) were investigated. As shown in Fig. 10(c), the content of RGO in the RGO-UiO-66(NH<sub>2</sub>) greatly influenced the photocatalytic activity, and it can be found that the optimal RGO content is 2%, for which the reduction ratio of Cr(VI) is even up to 100% after 100 min visible light illumination. Further increase of the RGO content in the RGO-UiO-66(NH<sub>2</sub>) led to a gradual decrease of the photocatalytic activity due to RGO shielding effect [176,177]. Also, excessive amount of RGO can mask the active sites on the surface of photoactive material, and increased amount of black color RGO further lowered the light intensity through the depth of reaction solution, thus resulting in the decreased performance of photocatalysts [177,178].

The mechanism of the Cr(VI) reduction over RGO-UiO-66(NH<sub>2</sub>) can be explained as the scheme of Fig. 13(f), in which the UiO-66(NH<sub>2</sub>) is excited by visible light irradiation and electron–hole pairs are formed. The photogenerated electrons can reduce Cr(VI) to Cr(III), and water molecules can be oxidized by the holes. When the RGO is introduced, those photogenerated electrons from conduction band of UiO-66(NH<sub>2</sub>) can inject into graphene, promoting the

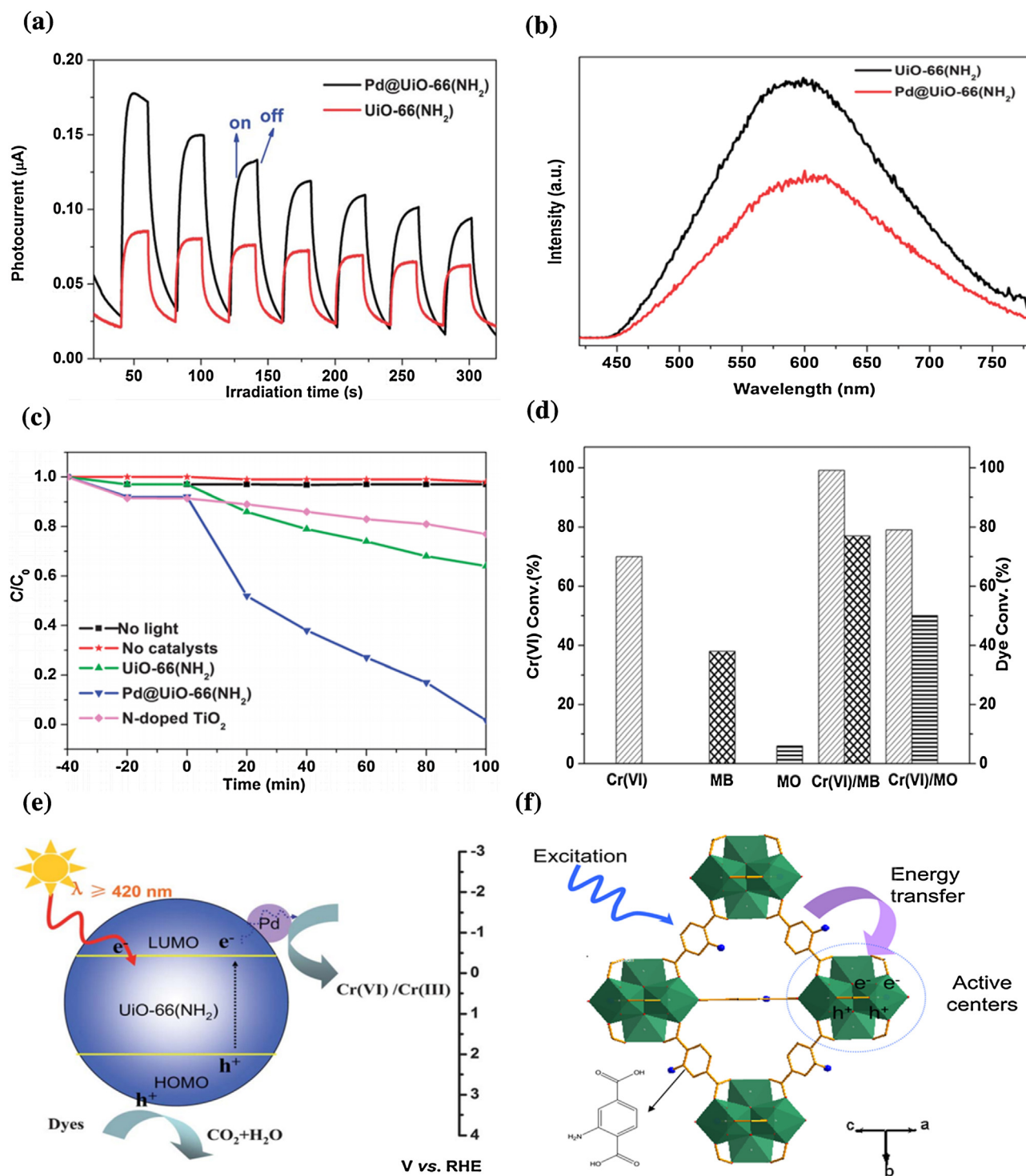


**Fig. 12.** (a) Transient photocurrent response of UiO-66(NH<sub>2</sub>) and Pd@UiO-66(NH<sub>2</sub>) in 0.2 M Na<sub>2</sub>SO<sub>4</sub> aqueous solution without bias versus Ag/AgCl under the irradiation of visible light (λ = 420 nm); (b) photoluminescence (PL) spectrum of UiO-66(NH<sub>2</sub>) and Pd@UiO-66(NH<sub>2</sub>); (c) reaction profiles of photocatalytic reduction of Cr(VI). Reaction conditions: 20 mg photocatalyst, 40 mL of 10 ppm Cr(VI), reaction temperature is 30 °C, pH = 2; (d) simultaneous photocatalytic reduction of Cr(VI) and degradation of dyes (10 ppm) on Pd@UiO-66(NH<sub>2</sub>) under visible light (λ = 420 nm) irradiation. Reaction conditions: 20 mg photocatalyst, 40 mL of 10 ppm Cr(VI), reaction temperature is 30 °C, reaction period is 60 min; (f) a schematic drawing of the structure of UiO-66(NH<sub>2</sub>) based on the structure of UiO-66. Zirconium-oxygen clusters (green part); N of the free amino groups (blue dots) [112], copyright (2013) Royal Society of Chemistry. (For interpretation of the references to colour in this figure legend, the reader is referred to the web version of this article.)

electron-hole pair separation. From this point, RGO acts as an electron collector and transporter to lengthen the lifetime of the charge carriers, consequently increasing the photocatalytic activity. The RGO in RGO-UiO-66(NH<sub>2</sub>) makes the photocatalytic reaction to take place not only on the surface of photocatalysts, but also on the RGO sheet, which enlarges the reaction space and offers more active sites

[178,179]. Similarly, the MIL-53(Fe)-RGO nanocomposites have also been successfully fabricated via an efficient electrostatic self-assembly method followed by a solvothermal reduction of GO to RGO [113]. MIL-53(Fe)-RGO nanocomposites exhibited considerable photocatalytic activity in the mixed systems (Cr(VI)/organic



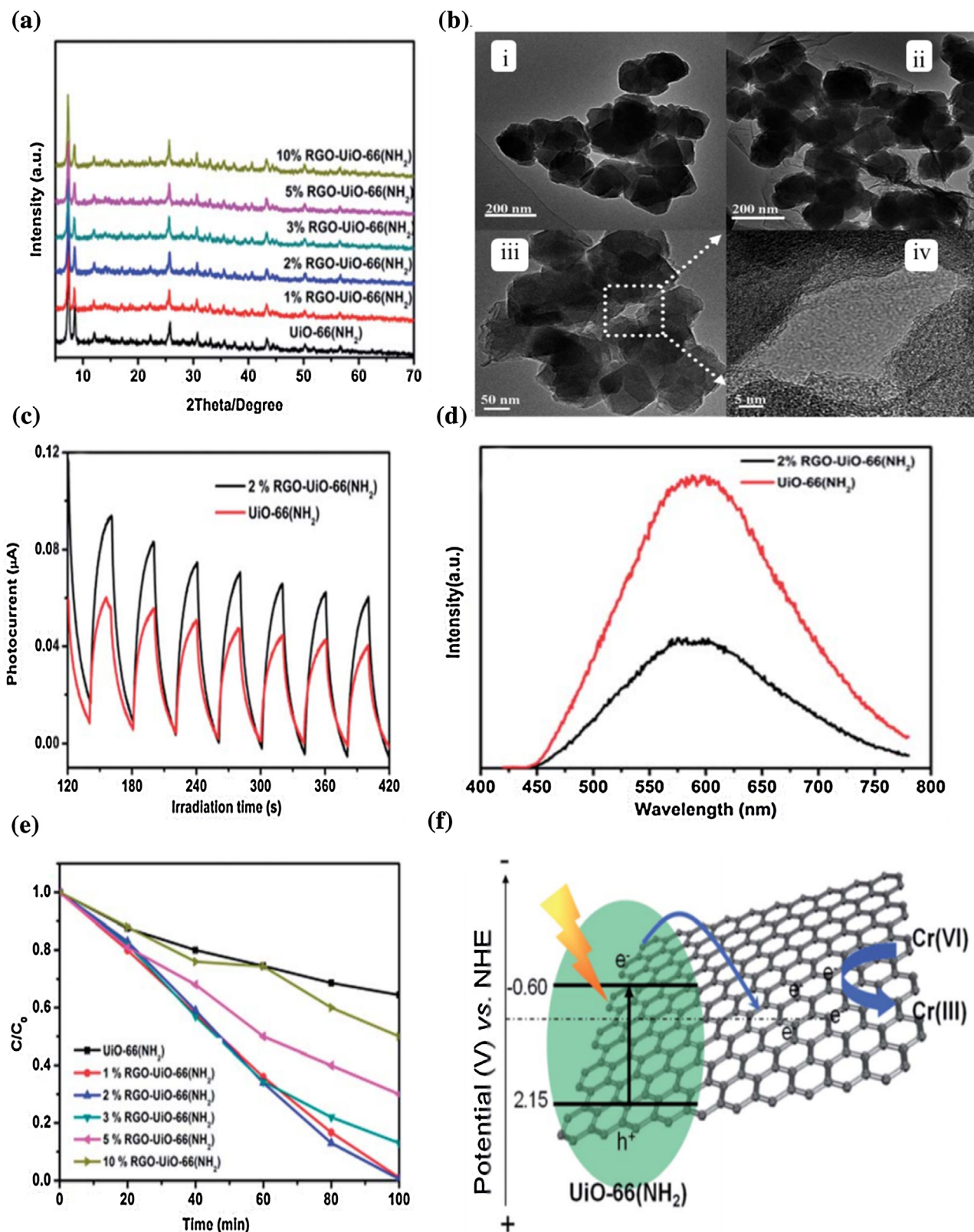


**Fig. 13.** (a) XRD patterns of the Uio-66(NH<sub>2</sub>) and RGO-Uio-66(NH<sub>2</sub>). (b) TEM images for the Uio-66(NH<sub>2</sub>) (i), RGO-Uio-66(NH<sub>2</sub>) (ii and iii), and HRTEM image of RGO-Uio-66(NH<sub>2</sub>) (iv). (c) Transient photocurrent response of the Uio-66(NH<sub>2</sub>) and RGO-Uio-66(NH<sub>2</sub>). (d) photoluminescence spectrum of the Uio-66(NH<sub>2</sub>) and RGO-Uio-66(NH<sub>2</sub>). (e) Photocatalytic reduction efficiency of aqueous Cr(VI) via RGO-Uio-66(NH<sub>2</sub>) with different RGO content. Reaction conditions: 20 mg photocatalyst, 40 mL of 10 ppm Cr(VI), reaction temperature 30 °C, pH = 2. (f) Possible mechanism of photocatalytic reduction of Cr(VI) over RGO-Uio-66(NH<sub>2</sub>) [111], copyright (2014) Royal Society of Chemistry.



**Table 4**Summary of surface area, pore volumes and pore sizes of the as-prepared UiO-66(NH<sub>2</sub>) and RGO-UiO-66(NH<sub>2</sub>) [111].

Sample	S <sub>BET</sub> (m <sup>2</sup> /g)	Total Pore Volume (cm <sup>3</sup> /g)	Average pore size (nm)
UiO-66(NH <sub>2</sub> )	732.21	0.089	4.11
1%RGO-UiO-66(NH <sub>2</sub> )	745.67	0.091	4.08
2%RGO-UiO-66(NH <sub>2</sub> )	766.54	0.095	4.09
3%RGO-UiO-66(NH <sub>2</sub> )	769.51	0.101	3.99
5%RGO-UiO-66(NH <sub>2</sub> )	788.51	0.14	5.11
10%RGO-UiO-66(NH <sub>2</sub> )	796.45	0.20	6.88

dyes), which made it a potential candidate for industrial wastewater treatment.

### 3. Challenges and outlooks

Up to now, it has been difficult to achieve high-throughput synthesis with amounts of kilogram quantities in relatively short time (a matter of hours) at ambient pressure. The solvothermal (including hydrothermal) methods, involving the use of an autoclave, and slow-diffusion processes will take days or weeks to complete, eliminating the possibility of an industrially relevant process [180,181]. Mechanochemical method was deemed as environment friendly way to yield quantitative products at room temperature under solvent (especially organic solvents) free conditions in short reaction times, normally in the range of 10–60 min [182–184]. But, it was not enough to characterize the samples obtained from mechanochemical method only via powder X-ray diffraction (XRD) analyses, due to that XRD was not sensitive to detect the presence of some low quantities of amorphous metal oxide phases or other crystalline phases which can be responsible for the catalytic activities observed [185]. The stability of MOFs during the photocatalytic process should be considered, because that the incidental pyrolyzation will cause damage to the framework of MOFs under high-intensity light irradiation because of the thermal effect of photons. In general, the thermal stability of MOFs is controlled by the coordination number and local coordination environment [186], therefore, it is very important to design and prepare MOFs with high thermal stability via optimizing coordination between the metal cluster and the organic linkers. In order to achieve higher photocatalytic efficiency, it is also necessary to expand MOFs' micropores into mesopores or to promote their electrical conductivity while maintaining the open diffusion channels and ensuring the mono-dispersion of metal centres [187,188]. To overcome the disadvantage of MOFs' poor electronic conductivity, it was suggested that doping can largely boost the electrical conductivity of MOFs based on the polarons/bipolarons and soliton mechanism [189]. Also, MOFs with 1D/2D structure can exhibit higher electrical conductivity in contrast to 3D frameworks [119,190]. From this point, further electronic band modulation and framework topology control of MOFs can possibly enhance photocatalytic properties in the solar-to-energy conversion. In addition, most MOFs also do not possess strong mechanical properties and good processability, all of which will hinder the integration of MOFs into functional solar devices [88].

Compared with other traditional photocatalysts like TiO<sub>2</sub>, CdS, ZnO, etc., a limited number of literatures were concerned to the MOFs as photocatalysts to perform Cr(VI) reduction. But, it was proved by these limited reports that MOFs can serve as promising photocatalysts to achieve Cr(VI) reduction, even also as dual-functional photocatalysts to degrade organic pollutants. The light absorption properties of this kind of photocatalysts can be improved through the simple modification of their organic ligands or doping with noble metal or GO. It is anticipated that these limited literatures on Cr(VI) reduction reaction with the aid of MOFs could provide new insight in the exploration and utilization of the MOFs, the development of property-controllable synthesis of pho-

tocatalysts, as well as the fabrication heterogeneous catalyst for solar-chemical energy conversion applications.

### Acknowledgements

We thank the financial support from National Natural Science Foundation of China (51578034), the Beijing Natural Science Foundation & Scientific Research Key Program of Beijing Municipal Commission of Education (KZ201410016018, KM201510016017), the Training Program Foundation for the Beijing Municipal Excellent Talents (2013D005017000004), the Importation & Development of High-Caliber Talents Project of Beijing Municipal Institutions (CIT&CD201404076), and the R&D Base Project for the Synergic Innovation Centre of Energy Saving and Carbon Emission Reduction under the Jurisdiction of Beijing Municipality (2016).

### Appendix A. Supplementary data

Supplementary data associated with this article can be found, in the online version, at <http://dx.doi.org/10.1016/j.apcatb.2016.04.030>.

### References

- [1] L. Järup, Br. Med. Bull. 68 (2003) 167–182.
- [2] H. Gu, S.B. Rapole, J. Sharma, Y. Huang, D. Cao, H.A. Colorado, Z. Luo, N. Haldolaarachchige, D.P. Young, B. Walters, RSC Adv. 2 (2012) 11007–11018.
- [3] J. Wang, K. Pan, E.P. Giannelis, B. Cao, RSC Adv. 3 (2013) 8978–8987.
- [4] B. Qiu, C. Xu, D. Sun, H. Wei, X. Zhang, J. Guo, Q. Wang, D. Rutman, Z. Guo, S. Wei, RSC Adv. 4 (2014) 29855–29865.
- [5] Y. Qu, W. Zhou, L. Jiang, H. Fu, RSC Adv. 3 (2013) 18305–18310.
- [6] Z. Lv, C. Liang, J. Cui, Y. Zhang, S. Xu, RSC Adv. 5 (2015) 18213–18217.
- [7] B.I. Kharisov, H.R. Dias, O.V. Kharissova, V.M. Jiménez-Pérez, B.O. Perez, B.M. Flores, RSC Adv. 2 (2012) 9325–9358.
- [8] P.Z. Ray, H.J. Shipley, RSC Adv. 5 (2015) 29885–29907.
- [9] S. Rengaraj, S. Venkataraj, J.-W. Yeon, Y. Kim, X. Li, G. Pang, Appl. Catal. B: Environ. 77 (2007) 157–165.
- [10] M. Owlad, M.K. Aroua, W.A.W. Daud, S. Baroutian, Water Air Soil Pollut. 200 (2009) 59–77.
- [11] C. Blöcher, J. Dorda, V. Mavrov, H. Chmiel, N. Lazaridis, K. Matis, Water Res. 37 (2003) 4018–4026.
- [12] F. Gode, E. Pehlivan, J. Hazard. Mater. 119 (2005) 175–182.
- [13] K. Selvi, S. Pattabhi, K. Kadirvelu, Bioresour. Technol. 80 (2001) 87–89.
- [14] C. Huang, M. Wu, Water Res. 11 (1977) 673–679.
- [15] S. Bai, T.E. Abraham, Bioresour. Technol. 79 (2001) 73–81.
- [16] S.E. Bailey, T.J. Olin, R.M. Bricka, D.D. Adrian, Water Res. 33 (1999) 2469–2479.
- [17] U. Divrikli, A.A. Kartal, M. Soyak, L. Elci, J. Hazard. Mater. 145 (2007) 459–464.
- [18] L. Khalil, W. Mourad, M. Rophael, Appl. Catal. B: Environ. 17 (1998) 267–273.
- [19] C. Chenthamarakshan, K. Rajeshwar, E.J. Wolfrum, Langmuir 16 (2000) 2715–2721.
- [20] Y. Ku, I.-L. Jung, Water Res. 35 (2001) 135–142.
- [21] L. Wang, N. Wang, L. Zhu, H. Yu, H. Tang, J. Hazard. Mater. 152 (2008) 93–99.
- [22] B. Xie, H. Zhang, P. Cai, R. Qiu, Y. Xiong, Chemosphere 63 (2006) 956–963.
- [23] X. Liu, L. Pan, T. Lv, G. Zhu, Z. Sun, C. Sun, Chem. Commun. 47 (2011) 11984–11986.
- [24] L. Yang, Y. Xiao, S. Liu, Y. Li, Q. Cai, S. Luo, G. Zeng, Appl. Catal. B: Environ. 94 (2010) 142–149.
- [25] J.A. Navío, G. Colon, M.A. Trillas, J. Peral, X. Domenech, J.J. Testa, J. Padron, D. Rodríguez, M.I. Litter, Appl. Catal. B: Environ. 16 (1998) 187–196.
- [26] B. Sun, E.P. Reddy, P.G. Smirniotis, Environ. Sci. Technol. 39 (2005) 6251–6259.
- [27] Y. Tian, L. Huang, X. Zhou, C. Wu, J. Hazard. Mater. 225 (2012) 15–20.

- [28] Y. Yang, M.H. Diao, M.M. Gao, X.F. Sun, X.W. Liu, G.H. Zhang, Z. Qi, S.G. Wang, *Electrochim. Acta* 132 (2014) 496–503.
- [29] L. Kakakel, G. Lutfullah, M.I. Bhanger, A. Shah, A. Niaz, J. Hazard. Mater. 148 (2007) 560–565.
- [30] J. Hu, G. Chen, I.M. Lo, *Water Res.* 39 (2005) 4528–4536.
- [31] H.-L. Ma, Y. Zhang, Q.-H. Hu, D. Yan, Z.-Z. Yu, M. Zhai, *J. Mater. Chem.* 22 (2012) 5914–5916.
- [32] K.C. Lai, I.M. Lo, *Environ. Sci. Technol.* 42 (2008) 1238–1244.
- [33] C.E. Barrera-Díaz, V. Lugo-Lugo, B. Bilyeu, *J. Hazard. Mater.* 223 (2012) 1–12.
- [34] A.C. Somenahally, J.J. Mosher, T. Yuan, M. Podar, T.J. Phelps, S.D. Brown, Z.K. Yang, T.C. Hazen, A.P. Arkin, A.V. Palumbo, *PLoS One* 8 (2013) e83909.
- [35] A.U. Chaudhari, S.R. Tapase, V.L. Markad, K.M. Kodam, *J. Hazard. Mater.* 262 (2013) 580–588.
- [36] J. Chung, R. Nerenberg, B.E. Rittmann, *Water Res.* 40 (2006) 1634–1642.
- [37] A. Janczyk, E. Krakowska, G. Stochel, W. Macyk, *J. Am. Chem. Soc.* 128 (2006) 15574–15575.
- [38] R. Wang, K. Hashimoto, A. Fujishima, M. Chikuni, E. Kojima, A. Kitamura, M. Shimohigoshi, T. Watanabe, *Nature* 388 (1997) 431–432.
- [39] G. Cappelletti, C. Bianchi, S. Ardizzzone, *Appl. Catal. B: Environ.* 78 (2008) 193–201.
- [40] M.N. Chong, B. Jin, C.W. Chow, C. Saint, *Water Res.* 44 (2010) 2997–3027.
- [41] H. Tong, S. Ouyang, Y. Bi, N. Umezawa, M. Oshikiri, J. Ye, *Adv. Mater.* 24 (2012) 229–251.
- [42] Y.C. Zhang, J. Li, M. Zhang, D.D. Dionysiou, *Environ. Sci. Technol.* 45 (2011) 9324–9331.
- [43] W. Yang, L. Zhang, Y. Hu, Y. Zhong, H.B. Wu, X.W.D. Lou, *Angew. Chem. Int. Ed.* 51 (2012) 11501–11504.
- [44] H. Yoneyama, Y. Yamashita, H. Tamura, *Nature* 282 (1979) 817–818.
- [45] L. Shi, T. Wang, H. Zhang, K. Chang, X. Meng, H. Liu, J. Ye, *Adv. Sci.* 2 (2015) 1500006.
- [46] S.Y. Reece, J.A. Hamel, K. Sung, T.D. Jarvi, A.J. Esswein, J.J. Pijpers, D.G. Nocera, *Science* 334 (2011) 645–648.
- [47] A. Fujishima, *Nature* 238 (1972) 37–38.
- [48] W.J. Youngblood, S.-H.A. Lee, Y. Kobayashi, E.A. Hernandez-Pagan, P.G. Hoertz, T.A. Moore, A.L. Moore, D. Gust, T.E. Mallouk, *J. Am. Chem. Soc.* 131 (2009) 926–927.
- [49] T. Ohno, L. Bai, T. Hisatomi, K. Maeda, K. Domen, *J. Am. Chem. Soc.* 134 (2012) 8254–8259.
- [50] T. Nakazono, A.R. Parent, K. Sakai, *Chem. Commun.* 49 (2013) 6325–6327.
- [51] T. Zhang, W. Lin, *Chem. Soc. Rev.* 43 (2014) 5982–5993.
- [52] C.-C. Wang, Y.-Q. Zhang, J. Li, P. Wang, *J. Mol. Struct.* 1083 (2015) 127–136.
- [53] C.-C. Wang, H.-Y. Li, G.-L. Guo, P. Wang, *Transit. Met. Chem.* 38 (2013) 275–282.
- [54] C.-C. Wang, G.-L. Guo, P. Wang, *Transit. Met. Chem.* (2013) 1–8.
- [55] C.-C. Wang, G. Guo, P. Wang, *J. Mol. Struct.* 1032 (2012) 93–99.
- [56] C.-C. Wang, Z. Wang, F. Gu, G. Guo, *J. Mol. Struct.* 1004 (2011) 39–44.
- [57] C.-C. Wang, P. Wang, G.-S. Guo, *Transit. Met. Chem.* 35 (2010) 721–729.
- [58] C.-C. Wang, Z. Wang, F. Gu, G. Guo, *J. Mol. Struct.* 979 (2010) 92–100.
- [59] J. Lee, O.K. Farha, J. Roberts, K.A. Scheidt, S.T. Nguyen, J.T. Hupp, *Chem. Soc. Rev.* 38 (2009) 1450–1459.
- [60] C.-Y. Sun, S.-X. Liu, D.-D. Liang, K.-Z. Shao, Y.-H. Ren, Z.-M. Su, *J. Am. Chem. Soc.* 131 (2009) 1883–1888.
- [61] R.J. Kuppler, D.J. Timmons, Q.-R. Fang, J.-R. Li, T.A. Makal, M.D. Young, D. Yuan, D. Zhao, W. Zhuang, H.-C. Zhou, *Coord. Chem. Rev.* 253 (2009) 3042–3066.
- [62] X.-S. Wang, S. Ma, D. Sun, S. Parkin, H.-C. Zhou, *J. Am. Chem. Soc.* 128 (2006) 16474–16475.
- [63] C.-C. Wang, J.-R. Li, X.-L. Lv, Y.-Q. Zhang, G. Guo, *Energy Environ. Sci.* 7 (2014) 2831–2867.
- [64] C.-C. Wang, H.-p. Jing, P. Wang, S.-j. Gao, *J. Mol. Struct.* 1080 (2015) 44–51.
- [65] C.-C. Wang, H.-p. Jing, P. Wang, *J. Mol. Struct.* 1074 (2014) 92–99.
- [66] H.-P. Jing, C.-C. Wang, Y.-W. Zhang, P. Wang, R. Li, *RSC Adv.* 4 (2014) 54454–54462.
- [67] J.-R. Li, J. Yu, W. Lu, L.-B. Sun, J. Sculley, P.B. Balbuena, H.-C. Zhou, *Nat. Commun.* 4 (2013) 1538.
- [68] J.-R. Li, J. Sculley, H.-C. Zhou, *Chem. Rev.* 112 (2011) 869–932.
- [69] J.-R. Li, H.-C. Zhou, *Nat. Chem.* 2 (2010) 893–898.
- [70] J.-R. Li, D.J. Timmons, H.-C. Zhou, *J. Am. Chem. Soc.* 131 (2009) 6368–6369.
- [71] J.-R. Li, R.J. Kuppler, H.-C. Zhou, *Chem. Soc. Rev.* 38 (2009) 1477–1504.
- [72] L. Pan, D.H. Olson, L.R. Ciemmlonski, R. Heddy, J. Li, *Angew. Chem.* 118 (2006) 632–635.
- [73] Y.-Q. Zhang, C. Wang, T. Zhu, P. Wang, S.-J. Gao, *RSC Adv.* 5 (2015) 45688–45692.
- [74] N.L. Rosi, J. Eckert, M. Eddaoudi, D.T. Vodak, J. Kim, M. O’Keeffe, O.M. Yaghi, *Science* 300 (2003) 1127–1129.
- [75] J.L. Rowsell, O.M. Yaghi, *Angew. Chem. Int. Ed.* 44 (2005) 4670–4679.
- [76] D.J. Collins, H.-C. Zhou, *J. Mater. Chem.* 17 (2007) 3154–3160.
- [77] S. Ma, H.-C. Zhou, *Chem. Commun.* 46 (2010) 44–53.
- [78] M. Peplow, *Nature* 520 (2015) 148–150.
- [79] K. Sumida, D.L. Rogow, J.A. Mason, T.M. McDonald, E.D. Bloch, Z.R. Herm, T.-H. Bae, J.R. Long, *Chem. Rev.* 112 (2011) 724–781.
- [80] Y. Mu, J. Fu, Y. Song, Z. Li, H. Hou, Y. Fan, *Cryst. Growth Des.* 11 (2011) 2183–2193.
- [81] A.R. Millward, O.M. Yaghi, *J. Am. Chem. Soc.* 127 (2005) 17998–17999.
- [82] J.M. Simmons, H. Wu, W. Zhou, T. Yildirim, *Energy Environ. Sci.* 4 (2011) 2177–2185.
- [83] C.-c. Wang, P. Wang, L.I. Feng, *Transit. Met. Chem.* 37 (2012) 225–234.
- [84] L.-B. Sun, J.-R. Li, W. Lu, Z.-Y. Gu, Z. Luo, H.-C. Zhou, *J. Am. Chem. Soc.* 134 (2012) 15923–15928.
- [85] Y. Xie, H. Yang, Z.U. Wang, Y. Liu, H.-C. Zhou, J.-R. Li, *Chem. Commun.* 50 (2014) 563–565.
- [86] H.-C. Zhou, J.R. Long, O.M. Yaghi, *Chem. Rev.* 112 (2012) 673–674.
- [87] C.-C. Wang, Y.-Q. Zhang, T. Zhu, X.-Y. Zhang, P. Wang, S.-J. Gao, *Polyhedron* 90 (2015) 58–68.
- [88] J.-L. Wang, C. Wang, W. Lin, *ACS Catal.* 2 (2012) 2630–2640.
- [89] T. Zhang, W. Lin, *Chem. Soc. Rev.* 43 (2014) 5982–5993.
- [90] S. Wang, X. Wang, *Small* 11 (2015) 3097–3112.
- [91] F.X. Llabrés i Xamena, A. Corma, H. Garcia, *J. Phys. Chem. C* 111 (2007) 80–85.
- [92] P. Mahata, G. Madras, S. Natarajan, *J. Phys. Chem. B* 110 (2006) 13759–13768.
- [93] J. Gascon, M.D. Hernández-Alonso, A.R. Almeida, G.P. van Klink, F. Kapteijn, G. Mul, *ChemSusChem* 1 (2008) 981–983.
- [94] S. Bordiga, C. Lamberti, G. Ricchiardi, L. Regli, F. Bonino, A. Damin, K.-P. Lillerud, M. Bjorgen, A. Zecchina, *Chem. Commun.* (2004) 2300–2301.
- [95] T. Tachikawa, J.R. Choi, M. Fujitsuka, T. Majima, *J. Phys. Chem. C* 112 (2008) 14090–14101.
- [96] P. Mahata, G. Madras, S. Natarajan, *Catal. Lett.* 115 (2007) 27–32.
- [97] M. Alvaro, E. Carbonell, B. Ferrer, F.X. Llabrés i Xamena, H. Garcia, *Chem. Eur. J.* 13 (2007) 5106–5112.
- [98] C.-C. Wang, J.-R. Li, X.-L. Lv, Y.-Q. Zhang, G. Guo, *Energy Environ. Sci.* 7 (2014) 2831–2867.
- [99] Z.L. Wu, C.H. Wang, B. Zhao, J. Dong, F. Lu, W.H. Wang, W.C. Wang, G.J. Wu, J.Z. Cui, P. Cheng, *Angew. Chem. Int. Ed.* 54 (2016), <http://dx.doi.org/10.1002/ange.201508325>.
- [100] M. Fuentes-Cabrera, D.M. Nicholson, B.G. Sumpter, M. Widom, *J. Chem. Phys.* 123 (2005) 124713–124715.
- [101] L. Shen, S. Liang, W. Wu, R. Liang, L. Wu, *Dalton Trans.* 42 (2013) 13649–13657.
- [102] H. Furukawa, K.E. Cordova, M. O’Keeffe, O.M. Yaghi, *Science* 341 (2013) 1230444.
- [103] M. Nasalevich, M. Van der Veen, F. Kapteijn, J. Gascon, *CrystEngComm* 16 (2014) 4919–4926.
- [104] S.-L. Li, Q. Xu, *Energy Environ. Sci.* 6 (2013) 1656.
- [105] A. Wang, Y. Zhou, Z. Wang, M. Chen, L. Sun, X. Liu, *RSC Adv.* 6 (2016) 3671–3679.
- [106] H. Wang, X. Yuan, Y. Wu, G. Zeng, X. Chen, L. Leng, Z. Wu, L. Jiang, H. Li, *J. Hazard. Mater.* 286 (2015) 187–194.
- [107] L. Shen, R. Liang, M. Luo, F. Jing, L. Wu, *Phys. Chem. Chem. Phys.* 17 (2015) 117–121.
- [108] R. Liang, L. Shen, F. Jing, W. Wu, N. Qin, R. Lin, L. Wu, *Appl. Catal. B: Environ.* 162 (2015) 245–251.
- [109] R. Liang, F. Jing, L. Shen, N. Qin, L. Wu, *J. Hazard. Mater.* 287 (2015) 364–372.
- [110] X. Wang, J. Liu, S. Leong, X. Lin, J. Wei, B. Kong, Y. Xu, Z.-X. Low, J. Yao, H.-T. Wang, *ACS Appl. Mater. Interfaces* (2016), <http://dx.doi.org/10.1021/acsami.1026b00028>.
- [111] L. Shen, L. Huang, S. Liang, R. Liang, N. Qin, L. Wu, *RSC Adv.* 4 (2014) 2546–2549.
- [112] L. Shen, W. Wu, R. Liang, R. Lin, L. Wu, *Nanoscale* 5 (2013) 9374–9382.
- [113] R. Liang, L. Shen, F. Jing, N. Qin, L. Wu, *ACS Appl. Mater. Interfaces* 7 (2015) 9507–9515.
- [114] M. Trivedi, A. Kumar, G. Singh, A. Kumar, N.P. Rath, *New J. Chem.* (2016), <http://dx.doi.org/10.1039/c1035nj02630j>.
- [115] M. Yadav, Q. Xu, *Chem. Commun.* 49 (2013) 3327–3329.
- [116] R. Liang, R. Chen, F. Jing, N. Qin, L. Wu, *Dalton Trans.* 44 (2015) 18227–18236.
- [117] P.L. Feng, J.J. Perry IV, S. Nikodemski, B.W. Jacobs, S.T. Meek, M.D. Allendorf, *J. Am. Chem. Soc.* 132 (2010) 15487–15489.
- [118] M. Dan-Hardi, C. Serre, T. Frot, L. Rozes, G. Maurin, C. Sanchez, G. Férey, *J. Am. Chem. Soc.* 131 (2009) 10857–10859.
- [119] Y. Li, H. Xu, S. Ouyang, J. Ye, *Phys. Chem. Chem. Phys.* (2016), <http://dx.doi.org/10.1039/C1035CP05885F>.
- [120] A. Schoedel, Z. Ji, O.M. Yaghi, *Nat. Energy* 1 (2016) 16034.
- [121] L. Cao, Z. Lin, F. Peng, W. Wang, R. Huang, C. Wang, J. Yan, J. Liang, Z. Zhang, T. Zhang, *Angew. Chem. Int. Ed.* (2016), <http://dx.doi.org/10.1002/anie.201602121>.
- [122] Z.-M. Zhang, T. Zhang, C. Wang, Z. Lin, L.-S. Long, W. Lin, *J. Am. Chem. Soc.* 137 (2015) 3197–3200.
- [123] Y. Fu, D. Sun, Y. Chen, R. Huang, Z. Ding, X. Fu, Z. Li, *Angew. Chem.* 124 (2012) 3420–3423.
- [124] J. Long, S. Wang, Z. Ding, S. Wang, Y. Zhou, L. Huang, X. Wang, *Chem. Commun.* 48 (2012) 11656–11658.
- [125] Y. Horiuchi, T. Toyao, M. Saito, K. Mochizuki, M. Iwata, H. Higashimura, M. Anpo, M. Matsuoka, *J. Phys. Chem. C* 116 (2012) 20848–20853.
- [126] H. Wang, X. Yuan, Y. Wu, X. Chen, L. Leng, G. Zeng, *RSC Adv.* 5 (2015) 32531–32535.
- [127] R. Liang, L. Shen, F. Jing, W. Wu, N. Qin, R. Lin, L. Wu, *Appl. Catal. B: Environ.* 162 (2015) 245–251.
- [128] H.-L. Ma, Y. Zhang, Q.-H. Hu, D. Yan, Z.-Z. Yu, M. Zhai, *J. Mater. Chem.* 22 (2012) 5914–5916.
- [129] J.H. Cavka, S. Jakobsen, U. Olsbye, N. Guillou, C. Lamberti, S. Bordiga, K.P. Lillerud, *J. Am. Chem. Soc.* 130 (2008) 13850–13851.
- [130] S. Pu, L. Xu, L. Sun, H. Du, *Inorg. Chem. Commun.* 52 (2015) 50–52.

- [131] D. Sun, Y. Fu, W. Liu, L. Ye, D. Wang, L. Yang, X. Fu, Z. Li, *Chem. Eur. J.* 19 (2013) 14279–14285.
- [132] C. Gomes Silva, I. Luz, F.X. Llabrés i Xamena, A. Corma, H. García, *Chem. Eur. J.* 16 (2010) 11133–11138.
- [133] A. Fujishima, T.N. Rao, D.A. Tryk, *J. Photochem. Photobiol. C: Photochem. Rev.* 1 (2000) 1–21.
- [134] L. Wang, X. Li, W. Teng, Q. Zhao, Y. Shi, R. Yue, Y. Chen, *J. Hazard. Mater.* 244 (2013) 681–688.
- [135] P. Horcajada, F. Salles, S. Wuttke, T. Devic, D. Heurtaux, G. Maurin, A. Vimont, M. Daturi, O. David, E. Magnier, N. Stock, Y. Filinchuk, D. Popov, C. Riekel, G. Férey, C. Serre, *J. Am. Chem. Soc.* 133 (2011) 17839–17847.
- [136] D. Sun, Y. Fu, W. Liu, L. Ye, D. Wang, L. Yang, X. Fu, Z. Li, *Chem. Eur. J.* 19 (2013) 14279–14285.
- [137] M. Alvaro, E. Carbonell, B. Ferrer, F.X. Llabrés i Xamena, H. García, *Chem. Eur. J.* 13 (2007) 5106–5112.
- [138] N. Wang, L. Zhu, K. Deng, Y. She, Y. Yu, H. Tang, *Appl. Catal. B: Environ.* 95 (2010) 400–407.
- [139] Y.C. Zhang, J. Li, H.Y. Xu, *Appl. Catal. B: Environ.* 123 (2012) 18–26.
- [140] A. Giannakas, M. Antonopoulou, C. Daikopoulos, Y. Deligiannakis, I. Konstantinou, *Appl. Catal. B: Environ.* 184 (2016) 44–54.
- [141] S. Saha, G. Das, J. Thote, R. Banerjee, *J. Am. Chem. Soc.* 136 (2014) 14845–14851.
- [142] X. Li, J. Zhu, H. Li, *Appl. Catal. B: Environ.* 123 (2012) 174–181.
- [143] Y. Yuan, H. Wang, Y. Wu, X. Chen, G. Zeng, L. Leng, C. Zhang, *Catal. Commun.* 61 (2015) 62–66.
- [144] X. Gao, H.B. Wu, L. Zheng, Y. Zhong, Y. Hu, X.W.D. Lou, *Angew. Chem.* 126 (2014) 6027–6031.
- [145] Y. Wang, W. Yang, L. Zhang, Y. Hu, X.W.D. Lou, *Nanoscale* 5 (2013) 10864–10867.
- [146] S. Wang, J. Li, X. Zhou, C. Zheng, J. Ning, Y. Zhong, Y. Hu, *J. Mater. Chem. A* 2 (2014) 19815–19821.
- [147] L. Mao, J. Li, Y. Xie, Y. Zhong, Y. Hu, *RSC Adv.* 4 (2014) 29698–29701.
- [148] S. Gadipelli, W. Travis, W. Zhou, Z. Guo, *Energy Environ. Sci.* 7 (2014) 2232–2238.
- [149] H. Wu, W. Zhou, T. Yildirim, *J. Am. Chem. Soc.* 129 (2007) 5314–5315.
- [150] Z. Zhang, S. Xian, H. Xi, H. Wang, Z. Li, *Chem. Eng. Sci.* 66 (2011) 4878–4888.
- [151] H. Bux, C. Chmelik, R. Krishna, J. Caro, *J. Membr. Sci.* 369 (2011) 284–289.
- [152] Y. Pan, Z. Lai, *Chem. Commun.* 47 (2011) 10275–10277.
- [153] M. Zhu, D. Srinivas, S. Bhogswararao, P. Ratnasamy, M.A. Carreon, *Catal. Commun.* 32 (2013) 36–40.
- [154] U.P. Tran, K.K. Le, N.T. Phan, *ACS Catal.* 1 (2011) 120–127.
- [155] G. Lu, J.T. Hupp, *J. Am. Chem. Soc.* 132 (2010) 7832–7833.
- [156] H. Sun, S. Liu, S. Liu, S. Wang, *Appl. Catal. B: Environ.* 146 (2014) 162–168.
- [157] C. Martínez, M. Fernández, J. Santaballa, J. Faria, *Appl. Catal. B: Environ.* 102 (2011) 563–571.
- [158] Y. Lai, M. Meng, Y. Yu, X. Wang, T. Ding, *Appl. Catal. B: Environ.* 105 (2011) 335–345.
- [159] J. Cravillon, S. Münzer, S.-J. Lohmeier, A. Feldhoff, K. Huber, M. Wiebcke, *Chem. Mater.* 21 (2009) 1410–1412.
- [160] J. Cravillon, R. Nayuk, S. Springer, A. Feldhoff, K. Huber, M. Wiebcke, *Chem. Mater.* 23 (2011) 2130–2141.
- [161] J. Yao, D. Dong, D. Li, L. He, G. Xu, H. Wang, *Chem. Commun.* 47 (2011) 2559–2561.
- [162] J. Yu, S. Zhuang, X. Xu, W. Zhu, B. Feng, J. Hu, *J. Mater. Chem. A* 3 (2015) 1199–1207.
- [163] Q. Yuan, L. Chen, M. Xiong, J. He, S.-L. Luo, C.-T. Au, S.-F. Yin, *Chem. Eng. J.* 255 (2014) 394–402.
- [164] N.A. Khan, B.K. Jung, Z. Hasan, S.H. Jhung, *J. Hazard. Mater.* 282 (2015) 194–200.
- [165] X. Wang, W. Cai, Y. Lin, G. Wang, C. Liang, *J. Mater. Chem.* 20 (2010) 8582–8590.
- [166] L. Lin, T. Zhang, H. Liu, J. Qiu, X. Zhang, *Nanoscale* 7 (2015) 7615–7623.
- [167] C.-H. Kuo, Y. Tang, L.-Y. Chou, B.T. Sneed, C.N. Brodsky, Z. Zhao, C.-K. Tsung, *J. Am. Chem. Soc.* 134 (2012) 14345–14348.
- [168] S. Wang, Z.H. Zhu, A. Coomes, F. Haghserehsht, G.Q. Lu, *J. Colloid Interface Sci.* 284 (2005) 440–446.
- [169] T. Zhou, Y. Du, A. Borgna, J. Hong, Y. Wang, J. Han, W. Zhang, R. Xu, *Energy Environ. Sci.* 6 (2013) 3229–3234.
- [170] K.S. Novoselov, A.K. Geim, S.V. Morozov, D. Jiang, Y. Zhang, S.V. Dubonos, I.V. Grigorieva, A.A. Firsov, *Science* 306 (2004) 666–669.
- [171] A.K. Geim, *Science* 324 (2009) 1530–1534.
- [172] X. An, J.C. Yu, *RSC Adv.* 1 (2011) 1426–1434.
- [173] L. Jia, D.-H. Wang, Y.-X. Huang, A.-W. Xu, H.-Q. Yu, *J. Phys. Chem. C* 115 (2011) 11466–11473.
- [174] N. Zhang, Y. Zhang, X. Pan, X. Fu, S. Liu, Y.-J. Xu, *J. Phys. Chem. C* 115 (2011) 23501–23511.
- [175] C. Petit, B. Mendoza, D. O'Donnell, T.J. Bandosz, *Langmuir* 27 (2011) 10234–10242.
- [176] M.-Q. Yang, B. Weng, Y.-J. Xu, *Langmuir* 29 (2013) 10549–10558.
- [177] Y. Zhang, N. Zhang, Z.-R. Tang, Y.-J. Xu, *ACS Nano* 6 (2012) 9777–9789.
- [178] J. Zhang, J. Yu, M. Jaroniec, J.R. Gong, *Nano Lett.* 12 (2012) 4584–4589.
- [179] Q. Li, B. Guo, J. Yu, J. Ran, B. Zhang, H. Yan, J.R. Gong, *J. Am. Chem. Soc.* 133 (2011) 10878–10884.
- [180] C.G. Carson, K. Hardcastle, J. Schwartz, X. Liu, C. Hoffmann, R.A. Gerhardt, R. Tannenbaum, *Eur. J. Inorg. Chem.* 2009 (2009) 2338–2343.
- [181] A.A. Adeyemo, I.O. Adeoye, O.S. Bello, *Toxicol. Environ. Chem.* 94 (2012) 1846–1863.
- [182] N. Stock, S. Biswas, *Chem. Rev.* 112 (2011) 933–969.
- [183] M.P. Batten, M. Rubio-Martinez, T. Hadley, K.-C. Carey, K.-S.L.A. Polyzos, M.R. Hill, *Curr. Opin. Chem. Eng.* 8 (2015) 55–59.
- [184] D.E. Crawford, J. Casaban, *Adv. Mater.* (2016), <http://dx.doi.org/10.1002/adma.201505352>.
- [185] D. Farrusseng, S. Aguado, C. Pinel, *Angew. Chem. Int. Ed.* 48 (2009) 7502–7513.
- [186] B. Mu, K.S. Walton, *J. Phys. Chem. C* 115 (2011) 22748–22754.
- [187] Y. Han, P. Qi, S. Li, X. Feng, J. Zhou, H. Li, S. Su, X. Li, B. Wang, *Chem. Commun.* 50 (2014) 8057–8060.
- [188] S. Bala, I. Mondal, A. Goswami, U. Pal, R. Mondal, *J. Mater. Chem. A* 3 (2015) 20288–20296.
- [189] D.Y. Lee, D.V. Shinde, S.J. Yoon, K.N. Cho, W. Lee, N.K. Shrestha, S.-H. Han, *J. Phys. Chem. C* 118 (2013) 16328–16334.
- [190] G. Givaja, P. Amo-Ochoa, C.J. Gómez-García, F. Zamora, *Chem. Soc. Rev.* 41 (2012) 115–147.